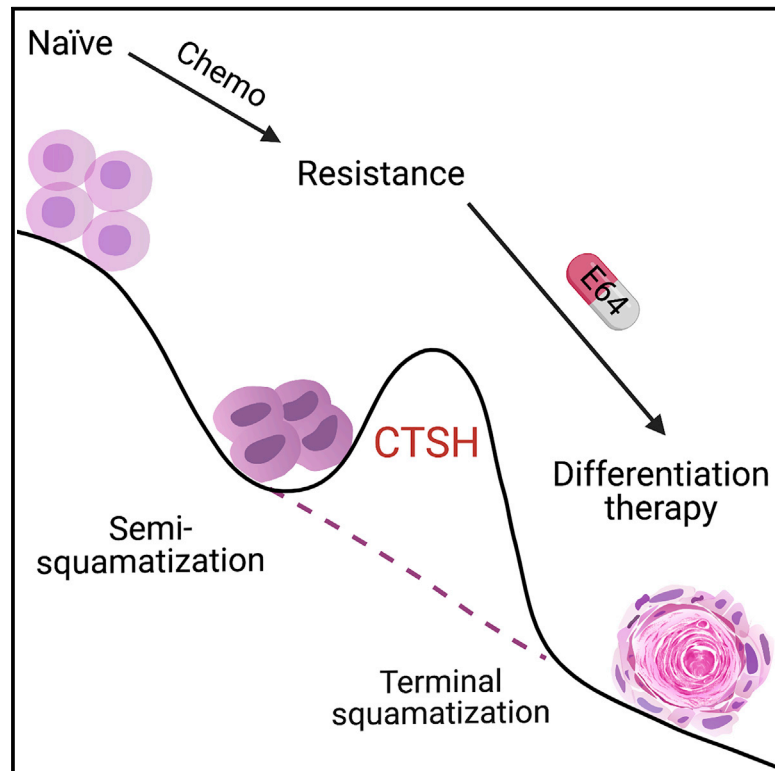


Acquired semi-squamization during chemotherapy suggests differentiation as a therapeutic strategy for bladder cancer

Graphical abstract



Authors

Manli Wang, Xuelan Chen, Ping Tan, ..., Yuquan Wei, Yu Liu, Chong Chen

Correspondence

weiqiang@scu.edu.cn (Q.W.),
yuliuscu@scu.edu.cn (Y.L.),
chongchen@scu.edu.cn (C.C.)

In brief

Wang et al. reveal that semi-squamization is a type of lineage plasticity associated with chemoresistance in muscle-invasive bladder cancer (MIBC). They find that targeting cathepsin H can induce the terminal squamous differentiation and thus specifically restrain the chemoresistant MIBC.

Highlights

- Chemotherapy leads to semi-squamization in MIBC
- Cathepsin H is essential for chemoresistant MIBC
- Cathepsin H inhibition induces terminal squamous differentiation
- The TNF pathway mediates the function of cathepsin H in MIBC



Article

Acquired semi-squamization during chemotherapy suggests differentiation as a therapeutic strategy for bladder cancer

Manli Wang,^{1,11} Xuelan Chen,^{2,11} Ping Tan,^{1,11} Yiyun Wang,^{2,11} Xiangyu Pan,² Tianhai Lin,¹ Yong Jiang,³ Bo Wang,² Huan Xu,³ Yuying Wang,² Yucen Yang,² Jian Wang,² Lei Zhao,² Jiapeng Zhang,¹ Ailing Zhong,² Yiman Peng,² Jiajia Du,² Qi Zhang,² Jianan Zheng,² Jingyao Chen,² Siqi Dai,² Feifei Na,⁴ Zhenghao Lu,⁵ Jiaming Liu,¹ Xiaonan Zheng,¹ Lu Yang,¹ Peng Zhang,¹ Ping Han,¹ Qiyong Gong,^{6,7} Qian Zhong,⁸ Kai Xiao,⁹ Hanshuo Yang,² Hongxin Deng,² Yinglan Zhao,² Hubing Shi,² Jianghong Man,¹⁰ Maling Gou,² Chengjian Zhao,² Lunzhi Dai,² Zhihong Xue,² Lu Chen,² Yuan Wang,² Musheng Zeng,⁸ Canhua Huang,² Qiang Wei,^{1,*} Yuquan Wei,² Yu Liu,^{2,*} and Chong Chen^{1,12,*}

¹Department of Urology, Institute of Urology, State Key Laboratory of Biotherapy and Cancer Center, Sichuan University, Chengdu, Sichuan 610041, China

²State Key Laboratory of Biotherapy and Cancer Center, West China Hospital, Sichuan University, Chengdu, Sichuan 610041, China

³Department of Pathology, West China Hospital, Sichuan University, Chengdu, Sichuan 610041, China

⁴Department of Thoracic Oncology, State Key Laboratory of Biotherapy and Cancer Center, West China Hospital, Sichuan University, Chengdu, Sichuan 610041, China

⁵Chengdu OrganoidMed Medical Laboratory, West China Health Valley, Chengdu, Sichuan 610041, China

⁶Huaxi MR Research Center (HMRR), Department of Radiology, West China Hospital, Sichuan University, Chengdu, Sichuan 610041, China

⁷Research Unit of Psychoradiology, Chinese Academy of Medical Sciences, Chengdu, Sichuan 610041, China

⁸State Key Laboratory of Oncology in South China, Collaborative Innovation Center for Cancer Medicine, Guangdong Key Laboratory of Nasopharyngeal Carcinoma Diagnosis and Therapy, Sun Yat-sen University Cancer Center, Guangzhou 510000, China

⁹Laboratory of Non-Human Primate Disease Model Research, State Key Laboratory of Biotherapy, Collaborative Innovation Center for Biotherapy, West China Hospital, Sichuan University, Chengdu 610041, China

¹⁰State Key Laboratory of Proteomics, National Center of Biomedical Analysis, Beijing 100850, China

¹¹These authors contributed equally

¹²Lead contact

*Correspondence: weiqiang@scu.edu.cn (Q.W.), yuliuscu@scu.edu.cn (Y.L.), chongchen@scu.edu.cn (C.C.)

<https://doi.org/10.1016/j.ccell.2022.08.010>

SUMMARY

Cisplatin-based chemotherapy remains the primary treatment for unresectable and metastatic muscle-invasive bladder cancers (MIBCs). However, tumors frequently develop chemoresistance. Here, we established a primary and orthotopic MIBC mouse model with gene-edited organoids to recapitulate the full course of chemotherapy in patients. We found that partial squamous differentiation, called semi-squamization, is associated with acquired chemoresistance in both mice and human MIBCs. Multi-omics analyses showed that cathepsin H (CTSH) is correlated with chemoresistance and semi-squamization. Cathepsin inhibition by E64 treatment induces full squamous differentiation and pyroptosis, and thus specifically restrains chemoresistant MIBCs. Mechanistically, E64 treatment activates the tumor necrosis factor pathway, which is required for the terminal differentiation and pyroptosis of chemoresistant MIBC cells. Our study revealed that semi-squamization is a type of lineage plasticity associated with chemoresistance, suggesting that differentiation via targeting of CTSH is a potential therapeutic strategy for the treatment of chemoresistant MIBCs.

INTRODUCTION

More than half a million people are diagnosed with bladder cancer each year, and approximately 40% of them die of it (Tran et al., 2021). Muscle-invasive bladder cancer (MIBC) is the most common and lethal type of bladder cancer. Despite recent progress in targeted therapy and immunotherapy, cisplatin-based chemotherapy is still the frontline treatment for unresect-

able and metastatic MIBCs. It is also increasingly used as neoadjuvant or adjuvant treatments before or after surgery and radiotherapy (Roupret et al., 2018). Unfortunately, most patients develop chemoresistance sooner or later.

Various mechanisms have been proposed for cancer chemoresistance, such as increased expressions of multidrug resistance genes, cell death inhibition, and enhanced DNA damage repair capacity (Vasan et al., 2019). Recent studies suggested



that cancer stem cells (CSCs) may play a critical role in chemoresistance (Batlle and Clevers, 2017; Coombs et al., 2017; Li et al., 2021; Valent et al., 2012). In bladder cancer, CSCs have been identified, which could be activated by prostaglandin E2 (Chan et al., 2009; Kurtova et al., 2015). However, the CSC hypothesis has been challenged by several lines of evidence. In some cancers, almost all tumor cells could perform like CSCs to regenerate tumors, and it has been shown that there is plasticity between CSCs and non-CSCs (Medema, 2013; Quintana et al., 2010).

Indeed, lineage plasticity, the ability of cancer cells to transit from one histological subtype to others, has been proposed to underlie treatment resistance in cancer (Le Magnen et al., 2018; Quintanal-Villalonga et al., 2020). For example, lung adenocarcinoma with *epidermal growth factor receptor* (EGFR) mutations could switch into neuroendocrine-like small-cell lung cancer after repeated EGFR inhibitor treatment (Oser et al., 2015; Sequist et al., 2011). Similarly, luminal prostate cancer can gain neuroendocrine phenotype after long-term antiandrogen treatment (Ku et al., 2017; Mu et al., 2017; Zou et al., 2017). Lineage plasticity has been less studied in bladder cancer (Sfakianos et al., 2020; Yang et al., 2020). However, it has been shown that there are several subtypes of MIBCs, including basal and luminal types, associated with distinct prognosis (Choi et al., 2014b; Robertson et al., 2017). It is believed that basal MIBCs may express high levels of stemness-related genes and display resistance to chemotherapy (Choi et al., 2014a; Tran et al., 2021). Of note, many of these basal MIBCs also expressed squamous markers. Sometimes, these bladder cancers were categorized as basal/squamous MIBCs, which has the worst prognosis.

In this study, we investigated whether lineage plasticity would contribute to chemoresistance in bladder cancer and thus give rise to susceptibility, by multi-omics and functional studies of both mouse and human MIBCs.

RESULTS

Generating primary and orthotopic MIBCs in mice with gene-edited bladder organoids

Several genetically engineered mouse models (GEMMs) of MIBCs have been reported (Kobayashi et al., 2015; Park et al., 2021; Puzio-Kuter et al., 2009; Ruan et al., 2019). However, these GEMMs are time-consuming, expensive, and not open to including additional genetic drivers. Therefore, we set out to generate primary, orthotopic, and drivers-defined MIBC mouse models with genome-edited bladder organoids in mice (Figure 1A). Bladder organoids were cultured from cyclic guanosine monophosphate (GMP)-AMP synthase (CGAS-Cas9) mice (Platt et al., 2014) (Figure S1A). Human MIBC-associated genetic alterations, including *Trp53* and *Pten* loss, were introduced into these organoids by CRISPR-Cas9 genome editing, together with *Myc* overexpression (transcripts per kilobase million [TPM]). Once orthotopically transplanted into the bladder of the recipient mice, these organoids survived and grew over time, as indicated by the *Myc*-linked luciferase living image (Figures 1B and S1B). The lesion was also observed at the transplant site by magnetic resonance imaging (Figure 1C). These mice had hematuria, a key clinic feature of bladder cancer patients (Figure 1D). Approximately 2 months after transplantation, all of the recipients died

of the disease, with enlarged bladders (Figures 1E, S1C, and S1D). Histological analyses confirmed a diagnosis of MIBC with tumor cells infiltrating into the muscle layers (Figure 1F). Tumor organoids could be generated from mice and maintain the pathologic features (Figures S1E and S1F). These mouse tumors specifically expressed the signature genes of human bladder cancer (Figure S1G). The luminal and squamous lineage signature genes were repressed, suggesting that these tumors were undifferentiated MIBCs (Figure S1H). Thus, we generated a primary and orthotopic MIBC mouse model with genetically engineered bladder organoids, which represented the histologic and molecular features of the human disease.

Recapitulating the full chemotherapy course of bladder cancer in mice

The mouse bladder cancers were treated with cisplatin plus gemcitabine. The growth of tumors with chemotherapy was significantly repressed after two treatments rounds (Figures 1G and 1H). However, all of them relapsed after 4–5 rounds of treatments. To test whether these relapsed tumors were resistant to chemotherapy, they were transplanted into the secondary recipients and further received chemotherapy. While the previously untreated tumors (sensitive) were significantly repressed by the treatment, the tumors from the relapsed donors displayed a minimal response (Figure 1I). This result indicated that the relapsed MIBCs acquired chemoresistance.

The chemosensitive and resistant tumors displayed distinct histology (Figure 1J). Chemoresistant tumors had fewer Ki67⁺ cells than the sensitive tumors, consistent with the generally slow cell cycle for chemoresistant cancers (Kurtova et al., 2015) (Figures S1I and S1J). Interestingly, the resistant tumors became positive for EPCAM, CK5, CK14, and p40 staining, markers for squamous cells, while most of the untreated tumor cells were negative (Figure S1I). Tumor organoids derived from sensitive and resistant tumors had distinct morphology that, while most of the sensitive tumor organoids were hollow, almost all of the resistant organoids were solid (Figures S1K and S1L). Consistent with the tumor tissues, the sensitive organoids were CK14[−], while the resistant ones were positive (Figures 1K and S1L). The half-maximal inhibitory concentration (IC₅₀) of the resistant organoids to cisplatin treatment was approximately a 4-fold increase compared to the sensitive ones (Figure S1M). The G2M checkpoint genes were significantly reduced, while the human MIBC chemoresistance-associated genes increased in mouse resistant tumors (Bucher and Britten, 2008) (Figure S1N). Thus, our mouse model faithfully recapitulated the full course of chemotherapy in human MIBCs.

Increased squamatization signature along the chemoresistance trajectory revealed by single-cell RNA sequencing (scRNA-seq)

To dissect the cellular and molecular changes in MIBCs along chemotherapy, we performed scRNA-seq analyses of the sensitive and resistant tumors. Each population was recognized with its conventional marker genes (Figures 2A and S2A; Table S1). On the combined t-distributed stochastic neighbor embedding (tSNE) plot, while most of the non-tumor cells from the sensitive and resistant tumors were largely overlapped, there were two distinct subpopulations, T1 and T2, which were dominant in

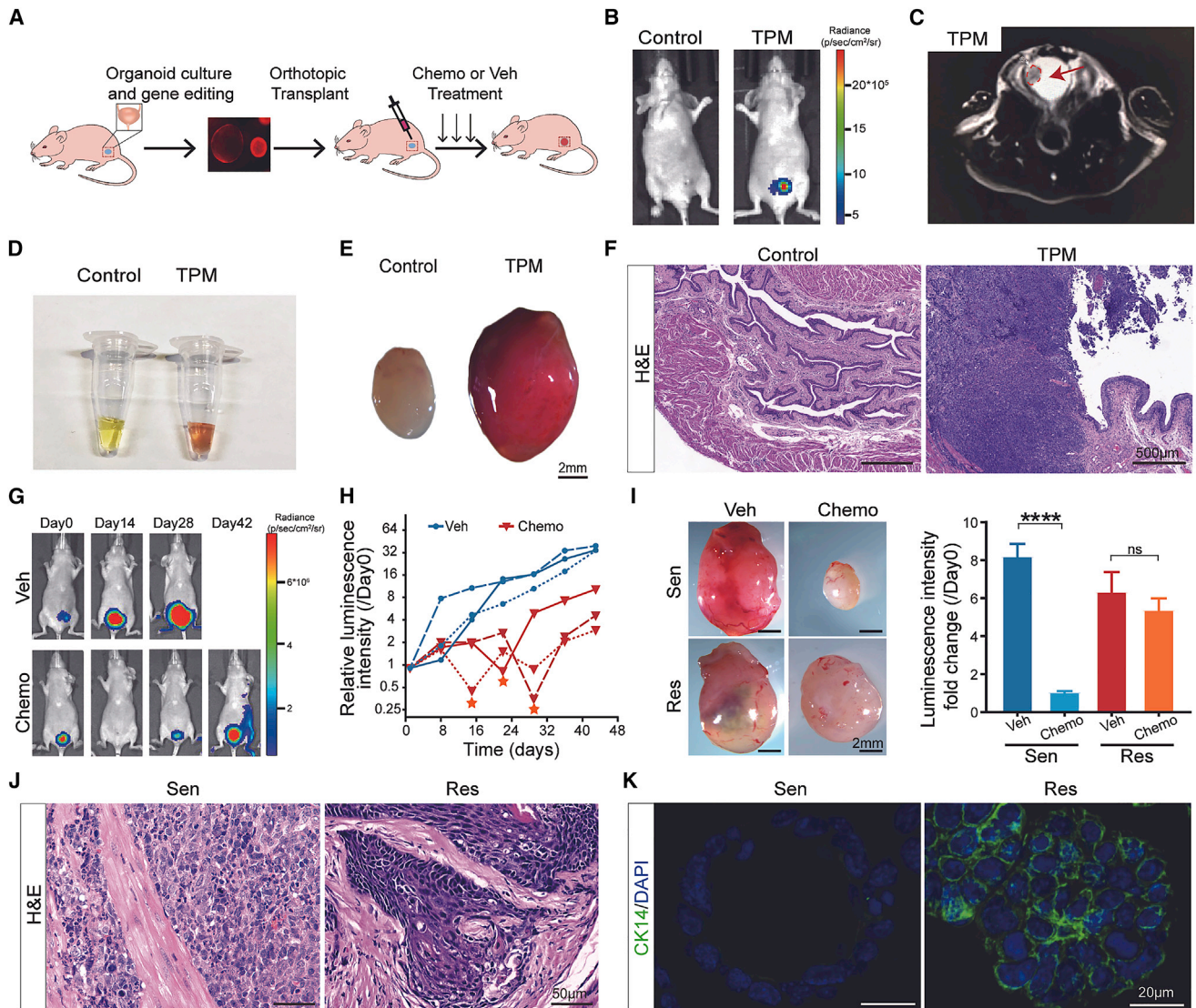


Figure 1. Generating a primary and orthotopic MIBC mouse model and recapitulating the full course of chemotherapy

(A) Schematic diagram of generating chemosensitive and chemoresistant orthotopic MIBCs in mice. (B and C) Bioluminescent images (B) (representative of $n = 6$ mice) and magnetic resonance image (C) (representative of $n = 6$ mice) of control or recipient mice at 20 days after being transplanted with sgTrp53, sgPten, and *Myc* (TPM) bladder organoids. (D) Image of urine from control and TPM mice at 20 d after transplantation (representative of $n = 6$ mice). (E) Bright-field image of the bladders of control and moribund recipient mice (representative of $n = 6$ mice). Scale bar, 2 mm. (F) H&E staining of normal bladder and that bearing TPM tumors (representative of $n = 6$ mice). Scale bars, 500 μm . (G) Bioluminescence images of mice with TPM tumors that received vehicle or chemotherapy (representative of $n = 3$ mice). (H) The luminescence intensity fold change of tumor-bearing mice during vehicle or chemotherapy. The stars indicate the best response of each mouse ($n = 3$ mice). (I) Bright-field images of bladders from chemosensitive (Sen) or chemoresistant (Res) tumors treated with vehicle or chemotherapy (left). The bar graph shows the luminescence intensity fold changes of chemosensitive or chemoresistant tumors that received vehicle or chemotherapy (right) (representative of $n = 3$ mice). Scale bars, 2 mm. **** $p < 0.0001$; ns, not significant. Two-sided Student's *t* test. Data presented as means \pm SEMs. (J and K) Images show H&E (J) and CK14 (K) staining of chemosensitive and chemoresistant tumors (representative of $n = 3$ mice). Scale bars, 50 μm (J) and 20 μm (K).

See also [Figure S1](#).

the sensitive and resistant tumors, respectively ([Figures 2B and S2B](#)). More T2 cells than T1 cells were at the G1 stage ([Figure S2C](#)).

To directly test whether the T1 cells were chemosensitive, while T2 cells were chemoresistant, we isolated them from the

sensitive and resistant tumors with the surface marker epithelial cellular adhesion molecule (EPCAM), a diagnostic marker associated with poor prognosis in bladder cancer ([Brunner et al., 2008](#); [Bryan et al., 2014](#)) ([Figures S2D and S2E](#)). T1 and T2 cells were purified according to their EPCAM expressions by flow

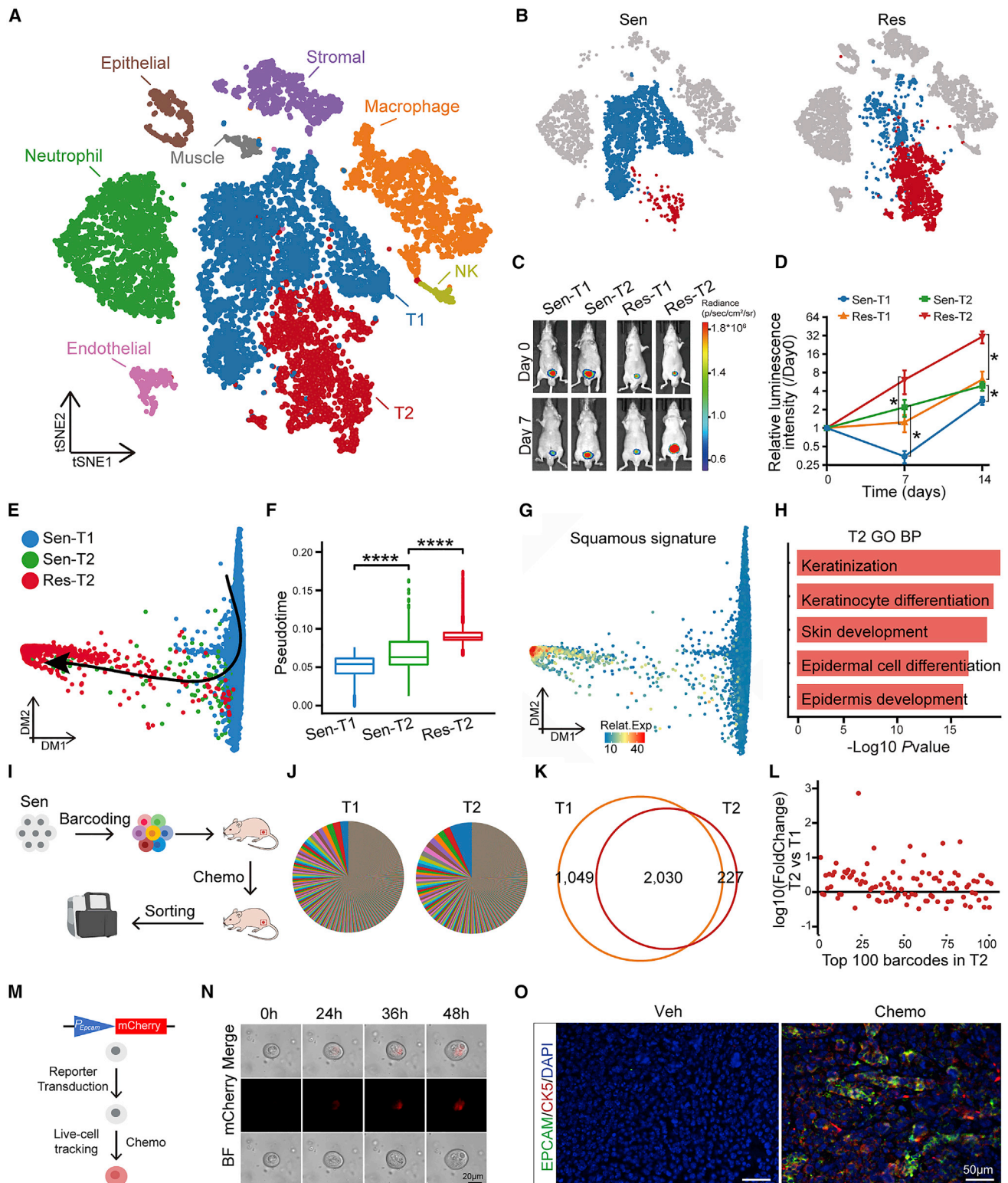


Figure 2. Squamous differentiation as a lineage plasticity of MIBC cells during chemotherapy

(A) t-SNE map of single-cell RNA-seq analyses of chemosensitive (Sen) and chemoresistant (Res) tumors from mice, colored by cell subtypes.

(B) t-SNE map shows the sample origins of tumor cells in (A).

(C) Luminescence images of mice transplanted with Sen-T1, Sen-T2, Res-T1, and Res-T2 tumor cells after once receiving chemotherapy (representative of n = 3 mice).

(legend continued on next page)

cytometry and then orthotopically transplanted into recipient mice (Figure S2F). The tumors derived from the Sen-T1 cells were significantly repressed by the treatment, while ones from the Res-T2 cells were not. Intriguingly, the response of the Sen-T2 and Res-T1 tumors was intermediate of the Sen-T1 tumors and the Res-T2 tumors (Figures 2C and 2D).

A chemoresistant trajectory was calculated from the T1 cells of the sensitive tumors, followed by the T2 cells of the sensitive tumors, to the T2 cells of the resistant tumors (Figures 2E and 2F). The dynamically expressed genes along the trajectory were identified and grouped into four modules (Figure S2G). The four module genes, continuously increased along the trajectory, were enriched in keratinocyte differentiation pathways (Figure S2G; Table S1). The squamous signature (Robertson et al., 2017; Sfakianos et al., 2020) was gradually upregulated along the trajectory (Figures 2G and S2H). Consistently, Gene Ontology (GO) analysis and gene set enrichment analysis (GSEA) showed that multiple gene sets related to keratinization and squamatization were significantly positively enriched in resistant tumors compared to sensitive ones, while in contrast, most of the stem cell-related gene sets were negatively enriched in the T2 cells (Figures 2H, S2I, and S2J; Table S1). In agreement with these molecular changes, the resistant tumors displayed obvious squamous differentiation histology, characterized with orderly arranged spindle nuclei, dyskeratosis, intracellular bridges, and nests of polygonal malignant cells (Figure 1J). These results strongly suggested that squamatization was associated with acquired chemoresistance in bladder cancer.

Lineage plasticity underlies acquired chemoresistance

To test whether the chemosensitive T1 cells could transit into chemoresistant T2 cells, we performed a barcoding assay. The chemosensitive tumor cells were labeled with DNA barcodes by lentivirus infection and transplanted into recipient mice. After a 14-day treatment, the T1 and T2 cells were purified by flow cytometry from mice with vehicle and chemotherapy, respectively, followed by deep sequencing (Figure 2I). The results showed that the T2 population maintained diversity similar to that of the T1 population (Figure 2J). A total of 65.9% of the barcodes in the T1 population were also presented in the T2 population (Figure 2K). No dominant clones were found in the T2 population (Figure 2L). Thus, lineage plasticity, but not a positive selection,

would underlie the transition from chemosensitive to resistant cells.

To directly visualize the transition, we applied live-cell tracking on single chemosensitive tumor organoids, which were transduced with a mCherry reporter driven by the *EPCAM* promoter (Figure 2M). mCherry⁺ cells were observed as early as 24 h after cisplatin treatment and the expression was further increased over time (Figure 2N). Furthermore, the T2-associated genes *Epcam*, *Krt5*, and *Ctsh* were significantly upregulated in both two-dimensional (2D) and 3D cultured T1 cell clones with chemotherapy, compared to their congenic ones with vehicle (Figure S2K). *In vivo*, the tumors derived from the purified Sen-T1 cells received vehicle or chemotherapy, and the vehicle-treated tumors remained EPCAM^{low}. In contrast, tumors treated with chemotherapy became EPCAM⁺ and CK5⁺ (Figure 2O). Taken together, these data strongly suggested that lineage plasticity to squamatization may underlie acquired resistance to chemotherapy in bladder cancer.

Acquired chemoresistance is accompanied by stepwise squamatization in mouse and human MIBCs

To mimic the multiple rounds of chemotherapy in clinical practice, we performed a serial chemotherapy experiment with the chemosensitive tumors in mice. RNA-seq and RT-qPCR showed that squamous signature genes were upregulated in the tumors treated twice with cisplatin and gemcitabine, compared to the sensitive tumors, and further upregulated in the tumors treated four times, compared to those treated twice (Figures 3A, S3A, and S3B; Table S2). Histologic analyses revealed the gradually squamous differentiation of the tumor cells after multiple rounds of chemotherapy, which was correlated with stepwise increased expressions of squamous markers CK5 and p40 (Figures 3B and S3C).

The patient-derived xenografts (PDXs) of human MIBCs also displayed gradually increased squamous features, indicated by increased expressions of squamous markers CK5 and p40, spindle-shaped nuclei, orderly arrangement of cells, intracellular bridges, and dyskeratosis (Figures 3C–3E; Table S3). The squamous gene signature and keratinocyte pathway were significantly positively enriched in PDX tumors with chemotherapy, compared to those treated with vehicle (Figure S3D). Then, we analyzed the biopsies of the same patients with MIBCs

(D) Relative luminescence intensity of Sen-T1, Sen-T2, Res-T1, and Res-T2 tumor-bearing mice with twice receiving chemotherapy (n = 3 mice). *p < 0.05. Two-sided Student's t test. Data presented as means ± SEMs.

(E) The diffusion map of mouse tumor cells, showing a chemosensitivity to chemoresistance trajectory. Colored by cell subtypes.

(F) Boxplot shows the pseudotime in different cell subtypes, measured by scRNA-seq analysis. ****p < 0.0001. Wilcoxon signed-rank test. Boxplots show the interquartile range (IQR) divided by the median. Whiskers represent the minimum and maximum values at 1.5*IQRs.

(G) The diffusion map of tumor cells, colored by the expression levels of squamous signature genes.

(H) Gene Ontology (GO) enrichment plot of the upregulated genes in T2 compared to T1 tumor cells.

(I) Schematic diagram of strategy for barcode-based lineage tracing.

(J) Pie charts show the barcode distribution in T1 (left) and T2 (right) tumor cells. Every single slice of the circle represents a barcode.

(K) Venn diagram shows overlapping of the barcodes in T1 and T2 tumor cells.

(L) Scatterplot shows the log₁₀-fold change of the top 100 barcodes in T2 tumor cells, compared to T1 tumor cells.

(M) Schematic diagram of strategy for single clone expansion for chemotherapy.

(N) Living images of chemosensitive human tumor organoid (patient 9) with *EPCAM*-promoter-mCherry reporter by 1 μM cisplatin treatment (representative of n = 3 technical replicates). Scale bar, 20 μm.

(O) EPCAM (green) and CK5 (red) staining of tumors derived from purified sorting Sen-T1 cells with vehicle or chemotherapy (representative of n = 3 mice). Scale bars, 50 μm.

See also Figure S2 and Tables S1 and S3.

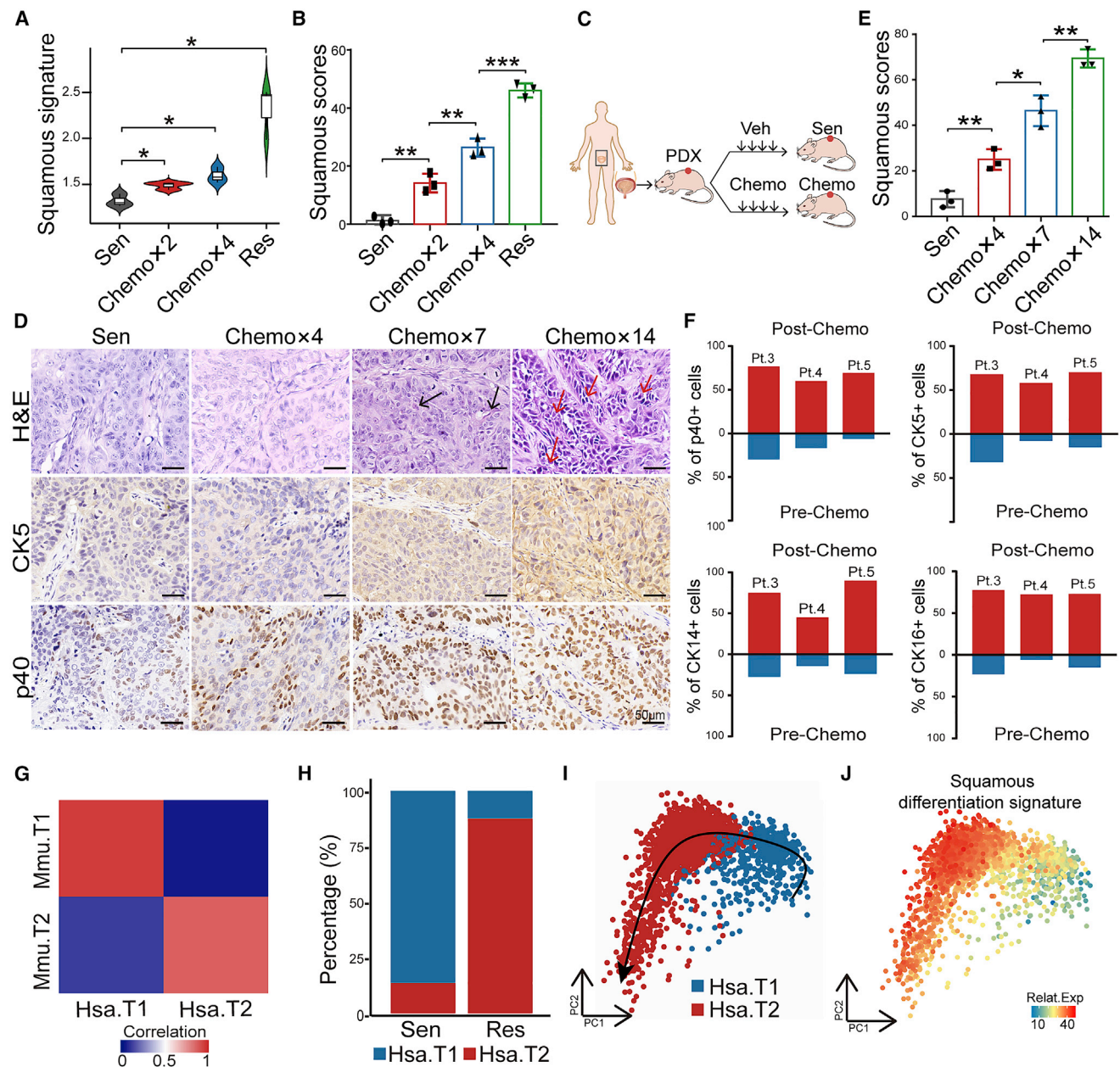


Figure 3. Chemotherapy induces stepwise squamatization in mouse and human MIBCs

(A) The relative expression levels of squamous signature genes in the sensitive, chemo×2, chemo×4, and resistant mouse MIBC, measured by bulk RNA-seq analysis (n = 3 mice). *p < 0.05. Two-sided Student's t test. Box shows the IQR divided by the median, Whiskers represent the minimum and maximum values at 1.5×IQRs.

(B) Statistical graphs show the combinatory squamous scores in the sensitive, chemo×2, chemo×4, and resistant mouse bladder tumors, quantified from immunohistochemistry (IHC) staining in Figure S3C (independent sections of n = 3 mice). **p < 0.01; ***p < 0.001. Two-sided Student's t test. Data presented as means ± SDs.

(C) Schematic diagram shows the serial chemotherapy in the human MIBC PDX model derived from human patients.

(D) H&E, CK5, and p40 staining of PDX tumors with different rounds of chemotherapy. Black arrow indicated dyskeratosis, and red arrow indicated intracellular bridges (representative of n = 3 mice). Scale bar, 50 μm.

(E) Statistical graphs show the squamous scores of PDX tumors with different rounds of chemotherapy, quantified from IHC staining in (D) (independent sections of n = 3 mice). *p < 0.05; **p < 0.01. Two-sided Student's t test. Data presented as means ± SDs.

(F) Statistical graphs show percentages of p40+, CK5+, CK14+, and CK16+ cells in biopsies of MIBC patients (patients 3–5) pre- and post-chemotherapy.

(G) Heatmap displays the correlation of patient T1 (Hsa.T1) and T2 (Hsa.T2) populations with mouse T1 (Mmu.T1) and T2 (Mmu.T2) populations (n = 1 mouse and n = 1 patient).

(H) The proportions of T1 and T2 tumor cells in sensitive (Sen) and resistant (Res) MIBC patients (n = 1 patient).

(legend continued on next page)

pre- and post-chemotherapy. All of the patients had enhanced levels of squamous markers, including p40, CK14, CK5, and CK16 after chemotherapy (Figures 3F and S3E).

We further performed scRNA-seq with tumor tissues directly from MIBC patients treated with or without chemotherapy (Figure S3F). Two subpopulations, human T1 and T2, of tumor cells could be recognized, highly similar to the T1 and T2 cells in mouse MIBCs, respectively, in terms of their gene expressions (Figure 3G; Table S3). The T1 cells were dominant in the tumors before chemotherapy, while the T2 cells in the tumors received chemotherapy (Figure 3H). The human T2 cells also expressed higher levels of *EPCAM* than the human T1 cells (Figure S3G). A pseudotime trajectory could be calculated from the T1 cells to T2 cells and The Cancer Genome Atlas (TCGA) drug-resistance gene signature was upregulated along the trajectory, and, of note, also the squamous differentiation signature (Figures 3I, 3J, and S3H; Table S2).

To directly test whether the human T1 cells could become squamous, we purified these *EPCAM*^{low} T1 cells from the untreated human MIBCs and then transplanted into NOD scid gamma (NSG) recipients, followed by vehicle or chemotherapy. After four rounds of chemotherapy, the majority of the tumor cells became *EPCAM*⁺ and *CK5*⁺, while those treated with vehicle were still negative for both markers (Figure S3I). Thus, both mouse and human MIBC cells underwent lineage plasticity during chemotherapy for acquired resistance.

Multi-omics profiling identifies cathepsin H (CTSH) as a key gene for chemoresistance

Assay for transposase-accessible chromatin with high-throughput sequencing (ATAC-seq) showed that the global chromatin accessibility was increased in the resistant tumor cells, which was significantly correlated with increased gene expressions (Figures S4A and S4B; Table S4). The genes with more open chromatin accessibility in the resistant cells were enriched in many squamatization and keratinocyte differentiation pathways (Figures 4A and S4C). All of the top positively enriched GO biological process (BP) pathways in the continuously upregulated genes (Bulk_sudo_Up) were related to keratinocyte differentiation (Figures S4D and S4E). These Bulk_sudo_Up genes were significantly overlapped with the genes upregulated along the chemoresistant trajectory (SC_sudo_Up, module 3 + module 4) (Figures 4B and S2G). The Bulk_sudo_Up and SC_sudo_Up genes significantly overlapped with the common_Up_1060 genes, and the resulting 93 (common_93) genes shared by all of them were also enriched in squamous differentiation (Figure 4B; Table S4). Mass spectrometry-based proteomics analyses showed that multiple squamous differentiation-related pathways were significantly enriched in the resistant tumors compared to the sensitive tumors at the protein level (Figure S4F). Among the common_93 genes upregulated at the chromosome and transcriptional levels, 50 genes were detected in proteomics, and 49 of them were also upregulated at the protein level, which included many very well-known squamous differen-

tiation-related genes, such as *SPRR1A/B*, *DSC1/2/3*, and *TGM1* (Figures 4C, S4G, and S4H; Table S5).

We noticed that CTSH, a lysosomal cysteine proteinase highly expressed in various human cancers (Olson and Joyce, 2015), was gradually upregulated along with the mouse and human chemoresistance trajectory (Figures 4D and 4E). It also stepwise increased in tumors with multiple rounds of chemotherapy at both mRNA and protein levels (Figures 4F–4H). In a cohort of MIBCs with chemotherapy (Faltas et al., 2016), the *CTSH* locus was amplified in 43.2% of patients after chemotherapy, but only 18.8% in those without chemotherapy (Figure S4I). In the TCGA BLCA cohort, patients with *CTSH* overexpression had a significantly increased TCGA_Resistance_UP gene signature and a significantly decreased Gemcitabine_Resistance_DN gene signature (Figure S4J). These patients, compared to those with *CTSH* downregulation, displayed significantly upregulated module 4 genes and significantly downregulated module 1 genes of the chemoresistance trajectory (Figures 4I and S4K). These data suggested that *CTSH* expression was correlated with chemoresistance in MIBCs.

CTSH is specifically required for chemoresistant MIBCs

To experimentally test its function in the chemoresistant MIBCs, *Ctsh* was disrupted in the organoids derived from the resistant tumors by CRISPR-Cas9 (Figure S4L). Compared to the scramble (Scr) single-guide RNA (sgRNA), sgRNAs targeting *Ctsh* significantly repressed the growth of the chemoresistant tumor organoids, indicated by reduced organoid numbers and size (Figures S4M and S4N). Once transplanted into the recipient mice, the tumors with sgCtsh were significantly smaller than the control tumors with sgScr (Figure 4J). The remaining sgCtsh tumors displayed distinct histology, characterized with increased cell death and lower density of tumor cells (Figure 4K). In contrast, *Ctsh* deficiency had a minimal effect on the growth of the chemosensitive MIBC organoids (Figure S4O). *In vivo*, the size of chemosensitive tumors with sgCtsh was comparable to that with sgScr (Figure S4P).

Then, we tested whether *Ctsh* was sufficient for chemoresistance by overexpressing it in the chemosensitive tumor organoids. The growth of the *Ctsh* overexpressed tumor organoids was comparable to the ones with vector only *in vitro* (Figure S4Q). However, the tumors with *Ctsh* overexpression relapsed earlier and grew significantly faster after chemotherapy than the control tumors *in vivo* (Figure 4L). *Ctsh* overexpression significantly increased the expressions of squamatization-related genes *Krt5* and *Krt14* (Figure 4M). Thus, CTSH was essential and sufficient for chemoresistance in MIBCs.

CTSH inhibitor E64 specifically represses the chemoresistant MIBCs and induces terminal squamous differentiation

The protease activity of CTSH could be effectively inhibited by E64, a compound first isolated from the fungus *Aspergillus violaceus* (Barrett et al., 1981, 1982). We treated the chemosensitive

(I) Principal-component analysis (PCA) map shows the cell subtypes of tumor cells derived from chemosensitive and resistant MIBC patients. The arrow indicates the pseudotime trajectory (n = 1 patient).

(J) PCA map of human MIBC tumor cells, colored by the expression levels of the squamous differentiation signature (n = 1 patient). See also Figure S3 and Tables S2 and S3.

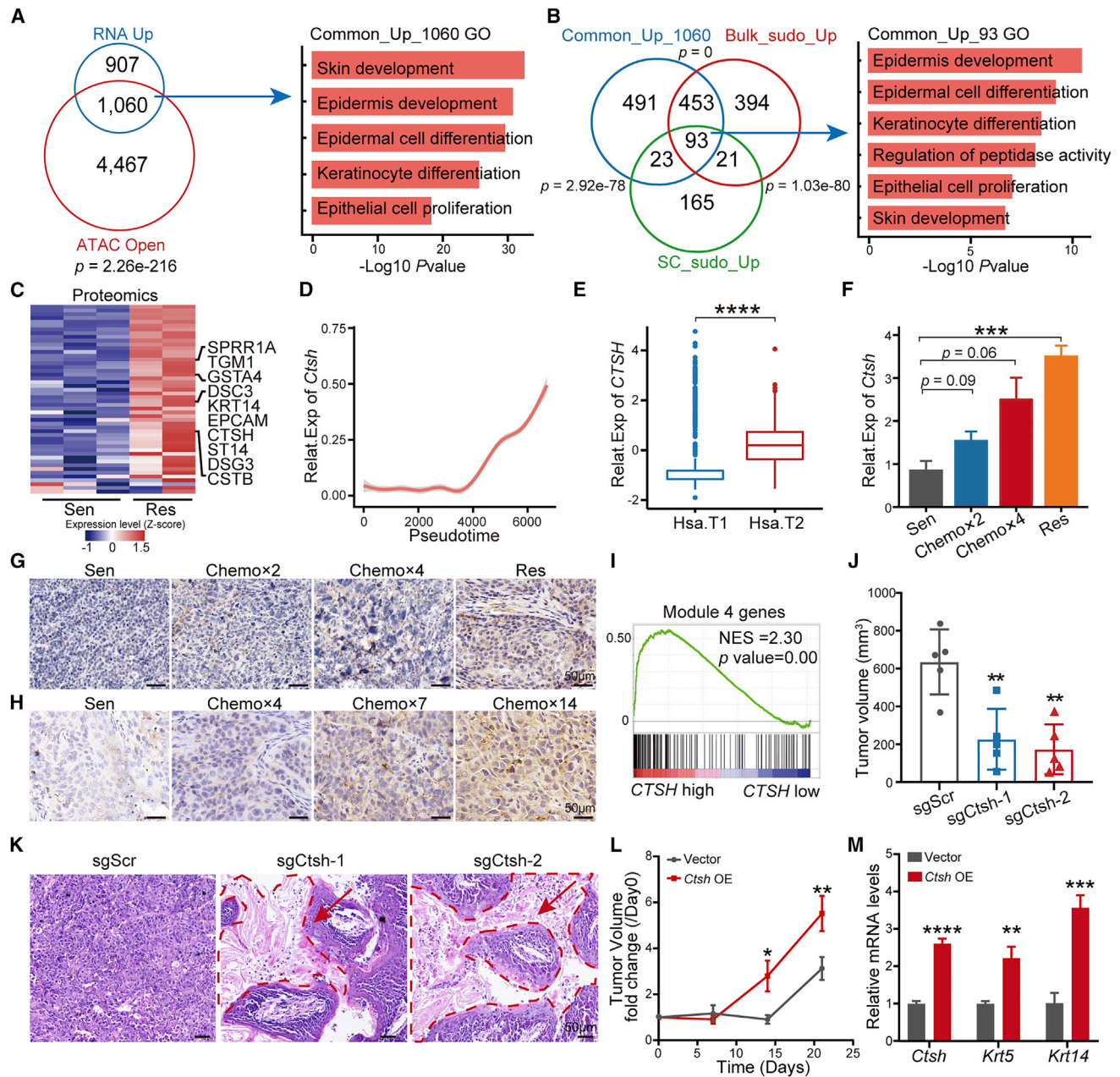


Figure 4. CTSH upregulation underlies MIBC chemoresistance

(A) Venn diagram shows overlapping of the chromatin open genes and upregulated genes in the chemoresistant cells compared to the sensitive cells. Hypergeometric test (left). The GO enrichment plot of the 1060 common_Up genes in the resistant cells (right).

(B) Venn diagram shows overlapping of common_Up_1060 genes in RNA-seq and ATAC-seq from (A), the module 3 and module 4 genes in the T1 to T2 tumor cell trajectory from Figure S2G (SC_sudo_Up), and the gradually increased genes in resistant samples, chemo×2 samples, and chemo×4 samples compared to sensitive samples (Bulk_sudo_Up). Hypergeometric test (left). The GO enrichment plot of the 93 common upregulated genes in the resistant cells (right).

(C) Heatmap shows the protein levels of the 50 genes of the common_Up_93 ones detected by MS proteomics (n = 3 mice [Sen], n = 2 mice [Res]).

(D) Dynamics of relative expression levels of *Ctsh* along with the chemoresistance trajectory of mouse MIBCs.

(E) Boxplot shows the relative expression levels of *CTSH* in human T1 and T2 tumor cells. ****p < 0.0001. Wilcoxon signed-rank test. Boxplots show the IQR divided by the median. Whiskers represent the minimum and maximum values at 1.5*IQRs.

(F) Bar graph shows the relative expression levels of *Ctsh* in the sensitive, chemo×2, chemo×4, and resistant samples, measured by bulk RNA-seq analysis (n = 3 mice). ***p < 0.0001. Two-sided Student's t test. Data presented as means ± SEMs.

(G and H) CTSH staining in mouse chemosensitive bladder tumors (G) (representative of n = 3 mice) and human PDX bladder tumors (patient 6) (H) (representative of n = 3 mice) with different rounds of chemotherapy. Scale bars, 50 μm.

(I) GSEA shows positive enrichment of the module 4 genes in the TCGA BLCA (n = 413 samples) with *CTSH* high expression, compared to those with *CTSH* low expression.

(legend continued on next page)

and resistant tumor organoids with E64 and found that the resistant ones were significantly more sensitive to E64 than the sensitive ones (Figure 5A). The bladders of the E64-treated mice were largely normal and significantly smaller than the control (Figures 5B and 5C). E64 treatment could also significantly repress the chemoresistant MIBC tumors subcutaneously transplanted into the recipient mice (Figure 5D). However, in contrast, it had no significant effect on the growth of the chemosensitive tumors (Figure 5E).

Pathologic analyses revealed that the E64-treated tumors displayed large areas of keratin pearls, concentric layers of keratin deposition, which were pink with H&E staining, and surrounded with hyperplasia of differentiated keratinocyte-like cells (Figures 5F and 5G). Involucrin, a specific marker for terminal differentiation of squamous cells and a component of the cornified cell envelope of the uppermost stratified epithelia, was expressed by the majority of the E64-treated tumor cells while completely absent in the tumors treated with vehicle (Carroll et al., 1993; Said et al., 1983; Walts et al., 1985). The remaining cells were CK16⁺, a marker for differentiating keratinocytes (de Jongh et al., 2005) (Figure 5F). However, keratin pearls were not observed in the chemosensitive tumors treated with either vehicle or E64 (Figure S5A). Consistently, *Ctsh* disruption by CRISPR/Cas9 also gave rise to significantly increased keratin pearls in the chemoresistant MIBC tumors, similar to those treated with E64 (Figures 4K and 5H).

Furthermore, both RNA-seq and mass spectrometry (MS) proteomics analyses showed that the chemoresistance gene signature was significantly negatively enriched in chemoresistant MIBCs treated with E64 compared to those with vehicle (Figures S5B and S5C). Given the protease activity of cathepsin, it was expected that multiple peptidase inhibitor activity pathways were upregulated by E64 treatment (Figure S5D; Table S6). Importantly, all of the top pathways enriched in E64-treated tumors, compared to those treated with vehicle, were related to keratinization, consistent with the pathological analyses (Figures 5I and 5J). Similarly, the expressions of multiple squamous differentiation-related genes increased in chemoresistant tumors with *Ctsh* loss (Figure 5K). Of note, the protein levels of squamous differentiation-related genes were mildly increased in the chemoresistant tumors compared to the chemosensitive ones and further increased by E64 treatment (Figure 5L; Table S5). The combinatory squamous signature was significantly higher in the chemoresistant tumors than those in the sensitive tumors and was further significantly increased by E64 treatment (Figures 5M and 5N). To distinguish the squamous differentiation of the chemoresistant MIBC cells and those after E64 treatment, we named the lineage transition of the chemoresistant cells from the chemosensitive ones semi-squamization.

scRNA-seq analyses of the vehicle and E64-treated chemoresistant tumors showed that the tumor subpopulation, called T3, emerged after E64 treatment (Figures S5E–S5G). The T3 tumor cells expressed significantly high levels of terminal squamous differentiation signature genes (Figure S5H). These data indicated that semi-squamization was strongly associated with chemoresistance in MIBCs, and CTSH inhibition could promote their fully squamous differentiation.

Differentiation therapy of chemoresistant human MIBCs

To test the potential differentiation therapy efficacy of E64 on human MIBCs, PDXs were established with tumor cells from MIBC patients in NSG mice (patients 7–9). PDXs of patients 7 and 8 expressed high levels of CTSH, similar to the PDX tumors of patient 6 (Res) with acquired chemoresistance, while the PDX tumors of patient 9 were CTSH⁻ (Figure S6A). Consistently, tumors derived from patients 7 and 8 had almost no response to chemotherapy, while the tumors of patient 9 were completely repressed (Figure S6B). E64 treatment significantly repressed the growth of the chemoresistant PDX tumors of patients 6 (Res), 7, and 8, while it had no significant effect on the growth of the chemosensitive tumors from patient 9 (Figures 6A and S6C). Organoids from patients 13 and 14 had significantly higher expression levels of *Ctsh* than chemosensitive organoids from patient 9 (Figure S6D). The organoids of patient 9 were sensitive to chemotherapy, while the organoids of patients 13 and 14 were chemoresistant (Figure S6E). In contrast, E64 treatment significantly inhibited the growth of organoids derived from patients 13 and 14 in a dose-dependent manner while having minimal effect on the ones from patient 9 (Figure S6F). Thus, E64 treatment could specifically inhibit the growth of both mouse and human chemoresistant MIBCs. Interestingly, these chemoresistant MIBC PDX tumors displayed large areas of keratin pearls after E64 treatment, suggesting terminal squamous differentiation. Immunofluorescence (IF) staining showed that E64-treated PDXs expressed high levels of involucrin, which was not expressed in vehicle-treated chemoresistant PDXs (Figure 6B). These results indicated that E64 could specifically repress chemoresistant MIBCs through terminal squamous differentiation.

Tumor necrosis factor (TNF) pathway is activated by CTSH inhibition and required for differentiation therapy in chemoresistant MIBCs

We wondered what the molecular mechanism underlying CTSH inhibition for the chemoresistant MIBCs might be. GSEA revealed that the TNF signaling pathway was significantly upregulated in E64-treated tumors compared to vehicle-treated ones at both transcription and protein levels (Figures 7A, S7A, and S7B; Table S6). The increased levels of TNF- α in the chemoresistant MIBC tumors treated with E64 were confirmed by western

(J) The tumor volume fold change of mouse chemoresistant MIBCs with sgScr or sgCtsh (n = 5 mice). **p < 0.01. Two-sided Student's t test. Data presented as means \pm SDs.

(K) H&E staining of mouse chemoresistant MIBCs with sgScr or sgCtsh. The arrow indicating keratin pearls (representative of n = 5 mice). Scale bars, 50 μ m.

(L) The tumor volume fold change of mouse chemosensitive tumors with or without *Ctsh* overexpression during 3 rounds of chemotherapy (n = 3 mice). *p < 0.05; **p < 0.01. Two-sided Student's t test. Data presented as means \pm SDs.

(M) The relative mRNA levels of *Ctsh*, *Krt5*, and *Krt14* in mouse chemosensitive tumors with or without *Ctsh* overexpression after 3 rounds of chemotherapy (n = 3 technical replicates) ****p < 0.0001; ***p < 0.001; **p < 0.01. Two-sided Student's t test. Data presented as means \pm SDs.

See also Figure S4 and Tables S3, S4, and S5.

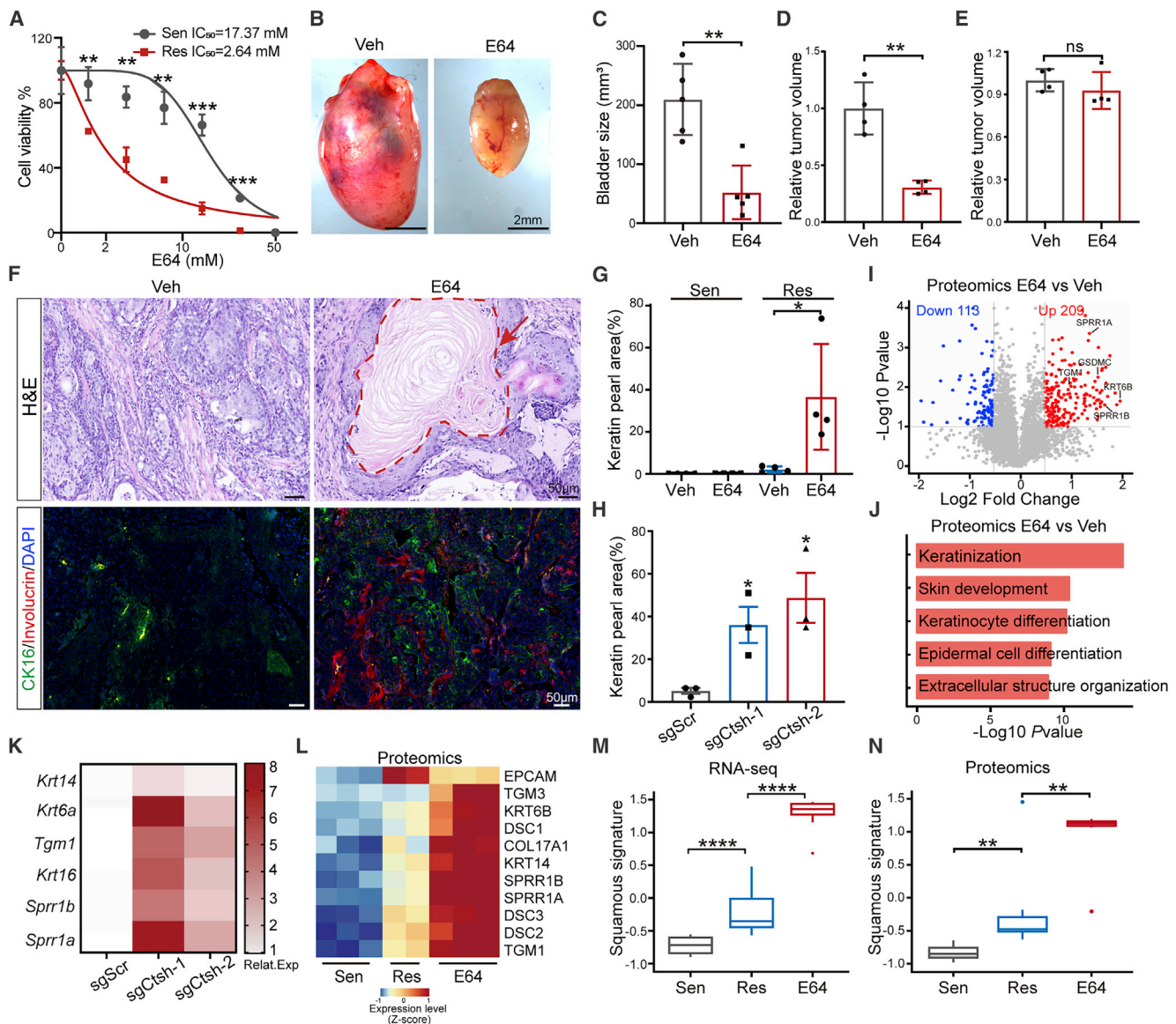


Figure 5. Inhibiting CTSH induces terminal squamous differentiation of chemoresistant MIBCs

(A) Dose-response curves of tumor organoids from chemosensitive and chemoresistant tumors treated with E64 ($n = 3$ technical replicates). ** $p < 0.01$; *** $p < 0.001$. Two-sided Student's t test. Data presented as means \pm SDs.

(B) Bright-field images of the bladders of chemoresistant MIBC mice treated with vehicle or E64 (representative of $n = 5$ mice). Scale bars, 2 mm.

(C) Statistical graphs show the size of the bladders of mice with orthotopic chemoresistant MIBCs treated with vehicle or E64 ($n = 5$ mice). ** $p < 0.01$. Two-sided Student's t test. Data presented as means \pm SDs.

(D and E) Bar graph shows the relative tumor volume (normalized to vehicle) of subcutaneous chemoresistant (D) or chemosensitive (E) tumors treated with vehicle or E64 ($n = 4$ mice). ** $p < 0.01$. ns, not significant. Two-sided Student's t test. Data presented as means \pm SDs.

(F) H&E (top) and immunofluorescence (IF; bottom) staining of CK16 (green) and involucrin (red) in mouse chemoresistant tumors with vehicle or E64 treatment (representative of $n = 4$ mice). Scale bars, 50 μ m.

(G) Bar graph shows the percentages of the keratin pearl area in mouse chemosensitive and chemoresistant tumors with or without E64 treatment (independent sections of $n = 4$ mice). * $p < 0.05$. Two-sided Student's t test. Data presented as means \pm SDs.

(H) Bar graph shows the percentages of the keratin pearl area in mouse chemoresistant tumors with sgScr or sgCtsh (independent sections of $n = 3$ mice). * $p < 0.05$. Two-sided Student's t test. Data presented as means \pm SDs.

(I) Volcano plot shows the differentially expressed proteins in chemoresistant tumor cells treated with E64, compared to those treated with vehicle, measured by MS proteomics assay.

(J) The GO enrichment plot of the upregulated genes in E64-treated chemoresistant tumor cells compared to vehicle-treated tumors, measured by MS proteomics assay.

(K) Relative expression levels of *Krt14*, *Krt6a*, *Tgm1*, *Krt16*, *Spr1b*, and *Spr1a* in mouse chemoresistant tumor organoids with sgScr or sgCtsh ($n = 3$ technical replicates).

(legend continued on next page)

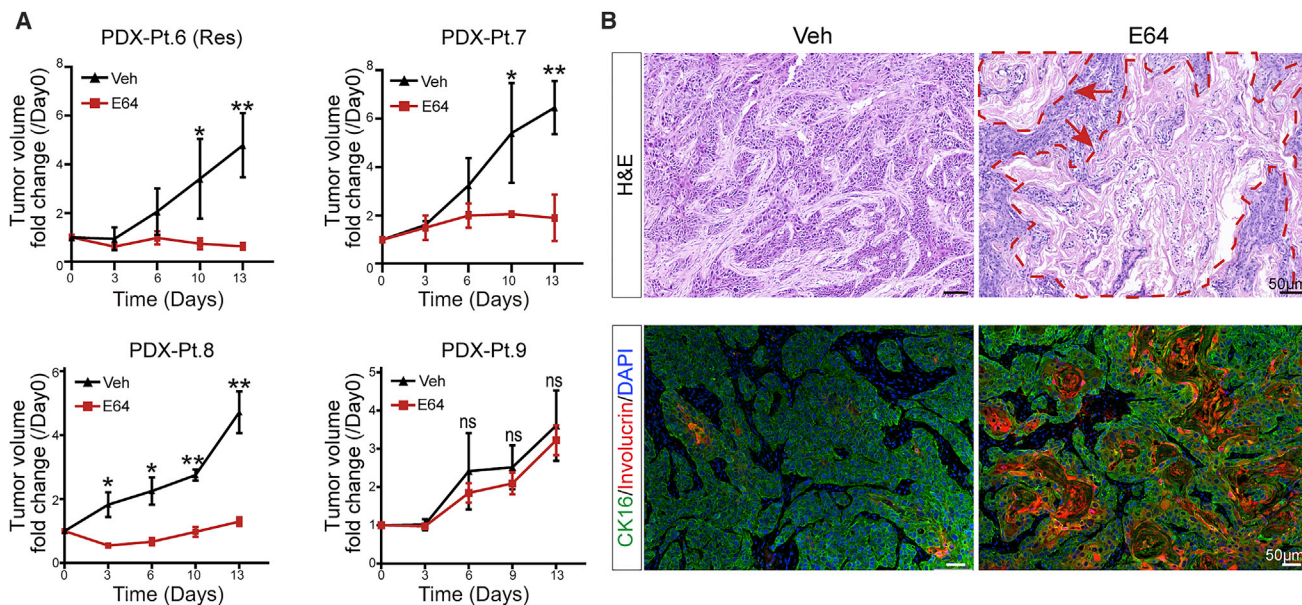


Figure 6. CTSH inhibition specifically represses human chemoresistant MIBCs

(A) Curves show the tumor volume fold change of PDX derived from chemoresistant MIBC patients (patients 6 [Res]–8) or a sensitive MIBC patient (patient 9) treated with vehicle or E64 treatment ($n = 3$ mice). * $p < 0.05$; ** $p < 0.01$; ns, not significant. Two-sided Student's *t* test. Data presented as means \pm SDs.

(B) H&E (top) and IF (bottom) staining of CK16 (green) and involucrin (red) in PDX tumors from patient 6 (Res) with vehicle or E64 treatment (representative of $n = 3$ mice). Scale bars, 50 μ m.

See also Figure S6 and Table S3.

blotting (Figure S7C). Recombinant TNF- α reduced the survival of the chemoresistant tumor organoids in a dose-dependent manner and significantly increased the expression levels of squamous differentiation-related genes, such as *Krt16*, *Krt6a*, *Spr1a*, and *Tgm1* (Figures S7D and S7E). *In vivo*, infliximab, a neutralizing antibody for both human and mouse TNF- α (Mitoma et al., 2018), completely blocked the effect of E64 treatment on chemoresistant tumors (Figure 7B). The E64 treatment-induced squamous pearls disappeared in the tumors treated with E64 plus infliximab. The terminal squamous differentiation marker involucrin was highly expressed in the tumors treated with E64 only, but not in those treated with both E64 and infliximab (Figure 7C).

Disrupting *Tnfr1*, a TNF- α receptor, with CRISPR-Cas9 moderately increased the numbers of chemoresistant tumor organoids cultured *in vitro* (Figure S7F). However, *Tnfr1* loss completely rescued the growth defects of the chemoresistant tumor organoids with sgCtsh (Figure 7D). The *in vivo* antitumor activity of E64 was significantly impaired by *Tnfr1* deficiency (Figures 7E and S7G). The keratin pearl formation was completely blocked by *Tnfr1* loss in the E64-treated tumors (Figures 7F and S7H). The expressions of squamous differentiation markers were also significantly reduced, consistent with the roles of TNF- α in the differentiation of epidermal keratinocytes

(Banno et al., 2004, 2005) (Figure S7H). In contrast, disruption of *Tnfr1* had minimal effect on the squamous differentiation of the chemoresistant tumors (Figures S7I and S7J). These data suggested that the TNF pathway was essential for the terminal squamous differentiation induced by E64 treatment in chemoresistant MIBCs.

Pyroptosis is induced and required for differentiation therapy of chemoresistant MIBCs

The cell death signature was specifically upregulated in the E64 treatment-specific T3 tumor cells (Figure S7K). GSEA showed that the pyroptosis pathway was significantly positively enriched in chemoresistant cells treated with E64 compared to those treated with vehicle (Figure S7L). Multiple pyroptosis genes, including *Gsdma*, *Gsdmb*, *Gsdmc*, and *Casp8*, were also upregulated at the protein level, revealed by proteomics analyses, by E64 treatment (Figure S7M; Table S5). Among them, gasdermin cells (GSDMCs) are not expressed in normal bladder epithelial cells but are highly expressed in skin and have been shown to be involved in breast cancer (Broz et al., 2020; Hou et al., 2020). We confirmed the increased levels of GSDMCs in the chemoresistant tumors treated with E64 by IF staining (Figure S7N). The cleaved GSDMC (GSDMC-N) was increased, while the full length of GSDMC was reduced in

(L) Heatmap shows the relative protein levels of squamous differentiation-related genes in the sensitive ($n = 3$ mice), resistant ($n = 2$ mice), and E64-treated resistant tumors ($n = 3$ mice), measured by MS proteomics assay.

(M and N) Boxplot shows the normalized expression levels of squamous signature in sensitive, resistant, and E64-treated resistant tumors, measured by bulk RNA-seq analysis (M) and MS proteomics assay (N) ($n = 3$ mice, Res group = 2 mice). ** $p < 0.01$; **** $p < 0.0001$. Two-sided Student's *t* test. Boxplots show the IQR divided by the median. Whiskers represent the minimum and maximum values at 1.5*IQRs.

See also Figure S5 and Tables S5 and S6.

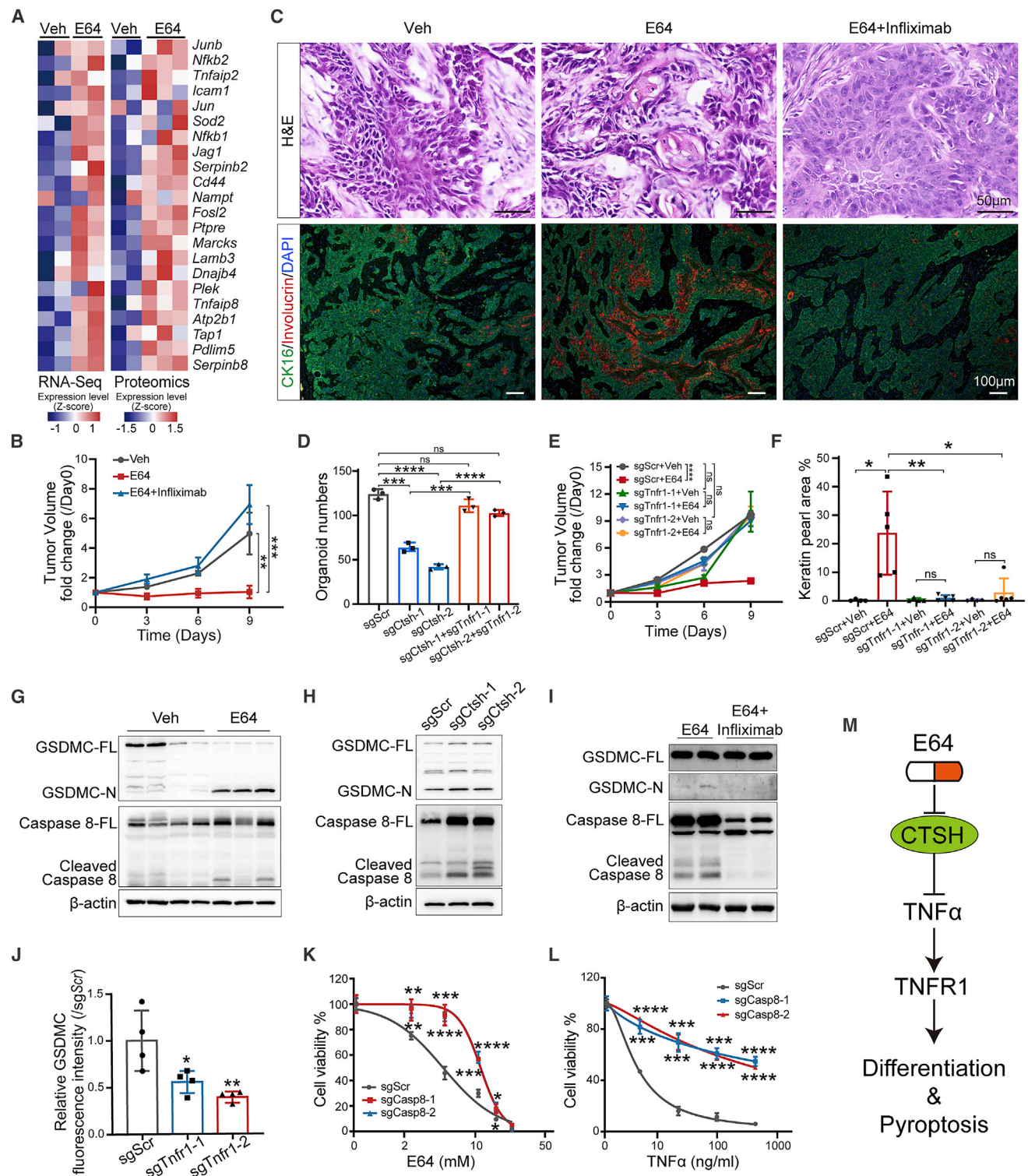


Figure 7. The TNF pathway is required for E64 treatment in MIBCs

(A) Heatmap shows the expression levels of genes related to the HALLMARK_TNFA_SIGNALING_VIA_NFKB pathway in chemoresistant tumor cells treated with vehicle or E64, measured by RNA-seq (left) and MS proteomics assay (right) (n = 2 mice, E64 group of MS proteomics, n = 3 mice).

(B) The curves show the fold change of tumor volumes of human chemoresistant tumors treated with vehicle, E64, or E64 plus infliximab (n = 4 mice). **p < 0.01; ***p < 0.001. Two-sided Student's t test. Data presented as Mean \pm SD.

(C) Images show H&E staining and IF staining of CK16 (green) and involucrin (red) of human chemoresistant tumors treated with vehicle, E64, or E64 plus infliximab (representative of n = 4 mice). Scale bars, 50 μ m (H&E) and 100 μ m (IF).

(legend continued on next page)

chemoresistant tumors by E64 treatment, together with increased cleaved caspase 8 (Figure 7G). Similarly, *Ctsh* loss also increased the cleavage of cCaspase 8 and GSDMCs (Figure 7H). Furthermore, E64 treatment induced the cleavage of caspase 8 and GSDMCs in human chemoresistant MIBCs treated with E64 (Figures S7O and S7P).

Pyroptosis can be activated by the TNF pathway through caspase 8 (Broz et al., 2020; Orning et al., 2018; Yu et al., 2021). In the E64-treated chemoresistant tumors, the cleavages of GSDMCs and caspase 8 were completely abolished by infliximab (Figure 7I). *Tnfr1* loss significantly reduced the levels of GSDMCs in the E64-treated tumors, as indicated by IF staining (Figure 7J). *Casp8* loss itself had minimal effect on the growth of these tumor organoids (Figure S7Q). However, tumor organoids with sgCasp8 were significantly more resistant to E64 treatment than the control organoids (Figure 7K). Similarly, they were also significantly more resistant to TNF- α treatment (Figure 7L). These data strongly suggested that caspase 8-mediated pyroptosis was essential for the CTSH-TNF- α /TNFR1-mediated differentiation therapy of the chemoresistant bladder cancer.

Our study revealed lineage plasticity of semi-squamization correlated with acquired chemoresistance in MIBCs. CTSH was required for the survival of chemoresistant tumor cells and targeting it with its inhibitor E64 led to terminal squamous differentiation and pyroptosis through the TNF pathway (Figure 7M).

DISCUSSION

Several types of cellular reprogramming have been proposed for tumorigenesis, metastasis, and treatment resistance (Le Magnen et al., 2018; Quintanal-Villalonga et al., 2020). Here, we show that in MIBCs treated with cisplatin-based chemotherapy, the basal tumor cells display squamous differentiation, instead of gaining stemness, indicated by their histology changes and squamous gene signature. We confirm that chemotherapy induces squamatization through lineage plasticity, which is consistent with the clinical observation that MIBC patients with squamous differentiation have a poor prognosis (Choi et al., 2014a, 2014b; Robertson et al., 2017). The underlying mechanisms for this lineage plasticity need further investigation and epigenetic and metabolic reprogramming

may be involved (DeBerardinis and Chandel, 2016; Jones and Baylin, 2002; Na et al., 2022; Pan et al., 2022). Of note, squamous differentiation associated with chemoresistance does not reach the terminal differentiation stage and is distinct from the squamous tumors with schistosomiasis, which may explain some controversies regarding the prognosis of bladder cancer with squamous differentiation (Li et al., 2017; Matulay et al., 2019). Therefore, semi-squamization, a previously unrecognized type of lineage plasticity, is a feature of acquired chemoresistance in MIBCs.

Lineage plasticity would lead to drug resistance, for the tumor cells may lose their dependence on the limited oncogenes and pathways of the original lineage (Le Magnen et al., 2018; Quintanal-Villalonga et al., 2020). In contrast, we propose that semi-squamization may give rise to susceptibility to differentiation therapy. Differentiation therapy was suggested half a century ago and one of the best examples may be the combination of retinoic acid and arsenic for acute promyelocytic leukemia (de The, 2018; Pierce and Wallace, 1971). Differentiation therapy has also been proposed for solid cancers, based on the hypothesis of CSCs, but there is little success (Cruz and Matushansky, 2012). However, in chemoresistant MIBCs, squamous differentiation has been initiated, although only halfway, and thus makes it more feasible to perform the terminal differentiation downhill from the Waddington landscape (Waddington, 1957). We show that the inhibition of CTSH, which is upregulated by chemotherapy and associated with semi-squamization in MIBCs, especially represses the growth of chemoresistant but not chemosensitive tumors through fully squamous differentiation. Our study provides an example that solid cancers can be effectively treated with differentiation therapy. It would be interesting to test whether this strategy would be applied to other epithelial cancers, especially in the case of lineage plasticity.

CTSH, together with other cathepsins, are generally upregulated in various cancers and associated with poor prognosis (Lah and Kos, 1998). Cathepsins may have profound effects on the tumorigenesis, metastasis, and treatment response of cancers (Olson and Joyce, 2015). Cathepsin C promotes the metastasis of breast cancer by recruiting neutrophils, and cathepsin L is associated with chemoresistance in neuroblastoma and ovarian cancer (Sui et al., 2016; Xiao et al., 2021; Zheng et al.,

(D) Organoid numbers of mouse chemoresistant tumor organoids with sgScr or sgCtsh or sgCtsh plus sgTnfr1 (n = 3 technical replicates). ****p < 0.0001; ***p < 0.001; ns, not significant. Two-sided Student's t test. Data presented as means \pm SDs.

(E) The curves show the fold change of tumor volumes of mouse chemoresistant tumors with sgScr or sgTnfr1 treated with vehicle or E64 (n = 4 mice). ****p < 0.0001; ns, not significant. Two-sided Student's t test. Data presented as means \pm SEMs.

(F) Bar graph shows the percentages of the keratin pearl area in mouse chemoresistant tumors with sgScr or sgTnfr1 treated with vehicle or E64 (independent sections of n = 4 mice). *p < 0.05; **p < 0.01. Two-sided Student's t test. Data presented as means \pm SDs.

(G) Western blotting plots of GSDMC and caspase 8 in mouse chemoresistant tumors treated with vehicle or E64 (n = 3 independent repeats).

(H) Western blotting plots of GSDMC and caspase 8 in mouse chemoresistant tumors with sgScr or sgCtsh (n = 3 independent repeats).

(I) Western blotting plots of GSDMC and caspase 8 in human chemoresistant tumors treated with E64 or E64 plus infliximab (n = 3 independent repeats).

(J) Statistical graph shows the relative GSDMC fluorescence intensity in chemoresistant tumors with sgScr or sgTnfr1 (independent sections of n = 4 mice). *p < 0.05; **p < 0.01. Two-sided Student's t test. Data presented as means \pm SDs.

(K) Dose-response curves of chemoresistant tumor organoids with sgScr or sgCasp8 treated with E64 (n = 3 technical replicates). *p < 0.05; **p < 0.01; ***p < 0.001; ****p < 0.0001. Two-sided Student's t test. Data presented as means \pm SDs.

(L) Dose-response curves of mouse chemoresistant tumor organoids with sgScr or sgCasp8 treated with TNF- α (n = 3 technical replicates). ***p < 0.001; ****p < 0.0001. Two-sided Student's t test. Data presented as means \pm SDs.

(M) The working model of blocking CTSH inducing differentiation and pyroptosis in chemoresistant bladder cancer.

See also Figure S7 and Tables S3, S5, and S6.

2004). CTSH is upregulated in high-grade bladder cancers and correlated with resistance to multiple drugs in human cancer cell lines (Dan et al., 2003; Staack et al., 2004). We find that CTSH is specifically essential for the survival of chemoresistant MIBC cells. Genetically or pharmaceutically inhibiting CTSH leads to terminal differentiation of these semi-squamization tumor cells through the TNF pathway, accompanied by pyroptosis. Given that several cathepsin inhibitors, including E64d, RWJ-445380, and MK0822, have been tested in clinical trials for various diseases and shown to have very low toxicity in humans, our study warrants a future clinical study to test the efficacy of the cathepsin inhibitors for chemoresistant MIBCs (Otto and Schirmeister, 1997; Palermo and Joyce, 2008).

STAR★METHODS

Detailed methods are provided in the online version of this paper and include the following:

- **KEY RESOURCES TABLE**
- **RESOURCE AVAILABILITY**
 - Lead contact
 - Materials availability
 - Data and code availability
- **EXPERIMENTAL MODEL AND SUBJECT DETAILS**
 - Human specimens
 - Mice
 - Cell culture
- **METHOD DETAILS**
 - Organoid culture
 - Organoid genome editing
 - Human MIBC sample processing
 - Mouse models establishment
 - *In vitro* treatment
 - *In vivo* treatment
 - MRI imaging and bioluminescent imaging
 - RNA extraction and RT-qPCR
 - Antibodies and reagents
 - Western blotting
 - H&E, immunohistochemistry and immunofluorescence
 - Squamous score evaluation
 - Keratin pearl area evaluation
 - Flow cytometry
 - Protein and peptide processing for mass spectrometry (MS)
 - Living image tracking
 - Bar-code-based lineage tracing
 - RNA-seq analyses
 - ATAC-seq analyses
 - Mass spectrometry (MS) data analysis
 - Single-cell RNA-seq analyses
 - Cell cycle analysis
 - The gene signature definition
- **QUANTIFICATION AND STATISTICAL ANALYSIS**

SUPPLEMENTAL INFORMATION

Supplemental information can be found online at <https://doi.org/10.1016/j.ccell.2022.08.010>.

ACKNOWLEDGMENTS

We thank all of the Chen and Liu lab members for discussion and technical support, the Core Facilities of West China Hospital, Sichuan University; Ms. Huifang Li for their technical support; and the Chengdu OrganoidMed Medical Laboratory. This study was supported by the National Key R&D Program of China (2017YFA0505600); the National Natural Science Foundation of China (82130007, 82170171, 82002692, 81770157, and 81522003); the Post-Doctoral Research Project of Sichuan University (grant no. 2021SCU12016); the Post-Doctoral Research Project, West China Hospital, Sichuan University (grant no. 19HXBH057); the “1.3.5” Project for Disciplines of Excellence, West China Hospital, Sichuan University (ZYJC21009, ZYYC20004, ZYGD18011, and ZY2016104); and the Sichuan Science and Technology Program (2020YFQ0059 and 2018JZ0077).

AUTHOR CONTRIBUTIONS

Conceptualization, C.C.; methodology, M.W., X.C., P.T., Y.W., X.P., T.L., Y.J., B.W., H.X., Y.W., Y.Y., J.W., L.Z., J. Zhang, A.Z., Y.P., J.D., Q. Zhang, J. Zheng, J.C., S.D., Z.L., F.N., J.L., X.Z., L.Y., P.Z., and P.H.; investigation, M.W., X.C., P.T., Y.W., X.P., T.L., Y.J., B.W., H.X., Y.W., Y.Y., J.W., L.Z., J. Zhang, A.Z., Y.P., J.D., Q. Zhang, J. Zhang, J.C., S.D., Z.L., F.N., J.L., X.Z., L.Y., P.Z., and P.H.; resources: Q.G., Q. Zhong, K.X., H.Y., H.D., Y.Z., H.S., J.M., M.G., C.Z., L.D., Z.X., L.C., Y.W., M.Z., and C.H.; Writing – original draft, M.W., X.C., P.T., Y.W., Y.L., and C.C.; Writing – review & editing, M.W., X.C., P.T., Y.W., Y.L., and C.C.; funding acquisition, Y.L. and C.C.; supervision, Q.W., Y.L., Y.W., and C.C.

DECLARATION OF INTERESTS

A patent (no. 202210623178.6) for the treatment of bladder cancer using cathepsin inhibitors has been issued by West China Hospital, Sichuan University.

Received: January 5, 2022

Revised: May 16, 2022

Accepted: August 11, 2022

Published: September 12, 2022

REFERENCES

- Banno, T., Gazel, A., and Blumenberg, M. (2004). Effects of tumor necrosis factor- α (TNF α) in epidermal keratinocytes revealed using global transcriptional profiling. *J. Biol. Chem.* 279, 32633–32642.
- Banno, T., Gazel, A., and Blumenberg, M. (2005). Pathway-specific profiling identifies the NF- κ B-dependent tumor necrosis factor α -regulated genes in epidermal keratinocytes. *J. Biol. Chem.* 280, 18973–18980.
- Barrett, A.J., Kembhavi, A.A., Brown, M.A., Kirschke, H., Knight, C.G., Tamai, M., and Hanada, K. (1982). L-trans-Epoxysuccinyl-leucylamido(4-guanidino) butane (E-64) and its analogues as inhibitors of cysteine proteinases including cathepsins B, H and L. *Biochem. J.* 207, 189–198.
- Barrett, A.J., Kembhavi, A.A., and Hanada, K. (1981). E-64 [L-trans-epoxysuccinyl-leucyl-amido(4-guanidino)butane] and related epoxides as inhibitors of cysteine proteinases. *Acta Biol. Med. Ger.* 40, 1513–1517.
- Battle, E., and Clevers, H. (2017). Cancer stem cells revisited. *Nat. Med.* 23, 1124–1134.
- Broz, P., Pelegrin, P., and Shao, F. (2020). The gasdermins, a protein family executing cell death and inflammation. *Nat. Rev. Immunol.* 20, 143–157.
- Brunner, A., Prelog, M., Verdorfer, I., Tzankov, A., Mikuz, G., and Ensinger, C. (2008). EpCAM is predominantly expressed in high grade and advanced stage urothelial carcinoma of the bladder. *J. Clin. Pathol.* 67, 307–310.
- Bryan, R.T., Shimwell, N.J., Wei, W., Devall, A.J., Pirrie, S.J., James, N.D., Zeegers, M.P., Cheng, K.K., Martin, A., and Ward, D.G. (2014). Urinary EpCAM in urothelial bladder cancer patients: characterisation and evaluation of biomarker potential. *Br. J. Cancer* 110, 679–685.
- Bucher, N., and Britten, C.D. (2008). G2 checkpoint abrogation and checkpoint kinase-1 targeting in the treatment of cancer. *Br. J. Cancer* 98, 523–528.

- Buenrostro, J.D., Giresi, P.G., Zaba, L.C., Chang, H.Y., and Greenleaf, W.J. (2013). Transposition of native chromatin for fast and sensitive epigenomic profiling of open chromatin, DNA-binding proteins and nucleosome position. *Nat. Methods* *10*, 1213–1218.
- Cao, J., Spielmann, M., Qiu, X., Huang, X., Ibrahim, D.M., Hill, A.J., Zhang, F., Mundlos, S., Christiansen, L., Steemers, F.J., et al. (2019). The single-cell transcriptional landscape of mammalian organogenesis. *Nature* *566*, 496–502.
- Carroll, J.M., Albers, K.M., Garlick, J.A., Harrington, R., and Taichman, L.B. (1993). Tissue- and stratum-specific expression of the human involucrin promoter in transgenic mice. *Proc. Natl. Acad. Sci. USA* *90*, 10270–10274.
- Chan, K.S., Espinosa, I., Chao, M., Wong, D., Ailles, L., Diehn, M., Gill, H., Presti, J., Jr., Chang, H.Y., van de Rijn, M., et al. (2009). Identification, molecular characterization, clinical prognosis, and therapeutic targeting of human bladder tumor-initiating cells. *Proc. Natl. Acad. Sci. USA* *106*, 14016–14021.
- Choi, W., Czerniak, B., Ochoa, A., Su, X., Siefker-Radtke, A., Dinney, C., and McConkey, D.J. (2014a). Intrinsic basal and luminal subtypes of muscle-invasive bladder cancer. *Nat. Rev. Urol.* *11*, 400–410.
- Choi, W., Porten, S., Kim, S., Willis, D., Plimack, E.R., Hoffman-Censits, J., Roth, B., Cheng, T., Tran, M., Lee, I.L., et al. (2014b). Identification of distinct basal and luminal subtypes of muscle-invasive bladder cancer with different sensitivities to frontline chemotherapy. *Cancer Cell* *25*, 152–165.
- Coombs, C.C., Zehir, A., Devlin, S.M., Kishtagari, A., Syed, A., Jonsson, P., Hyman, D.M., Solit, D.B., Robson, M.E., Baselga, J., et al. (2017). Therapy-related clonal hematopoiesis in patients with non-hematologic cancers is common and associated with adverse clinical outcomes. *Cell Stem Cell* *27*, 374–382.e4.
- Cruz, F.D., and Matushansky, I. (2012). Solid tumor differentiation therapy - is it possible? *Oncotarget* *3*, 559–567.
- Dan, S., Shirakawa, M., Mukai, Y., Yoshida, Y., Yamazaki, K., Kawaguchi, T., Matsuura, M., Nakamura, Y., and Yamori, T. (2003). Identification of candidate predictive markers of anticancer drug sensitivity using a panel of human cancer cell lines. *Cancer Sci.* *94*, 1074–1082.
- de Jongh, G.J., Zeeuwen, P.L.J.M., Kucharekova, M., Pfundt, R., van der Valk, P.G., Blokk, W., Dogan, A., Hiemstra, P.S., van de Kerkhof, P.C., and Schalkwijk, J. (2005). High expression levels of keratinocyte antimicrobial proteins in psoriasis compared with atopic dermatitis. *J. Invest. Dermatol.* *125*, 1163–1173.
- de The, H. (2018). Differentiation therapy revisited. *Nat. Rev. Cancer* *18*, 117–127.
- DeBerardinis, R.J., and Chandel, N.S. (2016). Fundamentals of cancer metabolism. *Sci. Adv.* *2*, e1600200.
- Dobin, A., Davis, C.A., Schlesinger, F., Drenkow, J., Zaleski, C., Jha, S., Batut, P., Chaisson, M., and Gingeras, T.R. (2013). STAR: ultrafast universal RNA-seq aligner. *Bioinformatics* *29*, 15–21.
- Faltas, B.M., Prandi, D., Tagawa, S.T., Molina, A.M., Nanus, D.M., Sternberg, C., Rosenberg, J., Mosquera, J.M., Robinson, B., Elemento, O., et al. (2016). Clonal evolution of chemotherapy-resistant urothelial carcinoma. *Nat. Genet.* *48*, 1490–1499.
- Gaspar, J.M. (2018). NGmerge: merging paired-end reads via novel empirically-derived models of sequencing errors. *BMC Bioinf.* *19*, 536.
- Hou, J., Zhao, R., Xia, W., Chang, C.W., You, Y., Hsu, J.M., Nie, L., Chen, Y., Wang, Y.C., Liu, C., et al. (2020). PD-L1-mediated gasdermin C expression switches apoptosis to pyroptosis in cancer cells and facilitates tumour necrosis. *Nat. Cell Biol.* *22*, 1264–1275.
- Jones, P.A., and Baylin, S.B. (2002). The fundamental role of epigenetic events in cancer. *Nat. Rev. Genet.* *3*, 415–428.
- Kobayashi, T., Owczarek, T.B., McKiernan, J.M., and Abate-Shen, C. (2015). Modelling bladder cancer in mice: opportunities and challenges. *Nat. Rev. Cancer* *15*, 42–54.
- Ku, S.Y., Rosario, S., Wang, Y., Mu, P., Seshadri, M., Goodrich, Z.W., Goodrich, M.M., Labbé, D.P., Gomez, E.C., Wang, J., et al. (2017). Rb1 and Trp53 cooperate to suppress prostate cancer lineage plasticity, metastasis, and antiandrogen resistance. *Science* *355*, 78–83.
- Kurtova, A.V., Xiao, J., Mo, Q., Pazhanisamy, S., Krasnow, R., Lerner, S.P., Chen, F., Roh, T.T., Lay, E., Ho, P.L., and Chan, K.S. (2015). Blocking PGE2-induced tumour repopulation abrogates bladder cancer chemoresistance. *Nature* *517*, 209–213.
- Lah, T.T., and Kos, J. (1998). Cysteine proteinases in cancer progression and their clinical relevance for prognosis. *Biol. Chem.* *379*, 125–130.
- Langmead, B., and Salzberg, S.L. (2012). Fast gapped-read alignment with Bowtie 2. *Nat. Methods* *9*, 357–359.
- Le Magnen, C., Shen, M.M., and Abate-Shen, C. (2018). Lineage plasticity in cancer progression and treatment. *Annu. Rev. Cancer Biol.* *2*, 271–289.
- Li, G., Yu, J., Song, H., Zhu, S., Sun, L., Shang, Z., and Niu, Y. (2017). Squamous differentiation in patients with superficial bladder urothelial carcinoma is associated with high risk of recurrence and poor survival. *BMC Cancer* *17*, 530.
- Li, H., Handsaker, B., Wysoker, A., Fennell, T., Ruan, J., Homer, N., Marth, G., Abecasis, G., and Durbin, R.; 1000 Genome Project Data Processing Subgroup (2009). The sequence alignment/map format and SAMtools. *Bioinformatics* *25*, 2078–2079.
- Li, W., Xu, H., Xiao, T., Cong, L., Love, M.I., Zhang, F., Irizarry, R.A., Liu, J.S., Brown, M., and Liu, X.S. (2014). MAGeCK enables robust identification of essential genes from genome-scale CRISPR/Cas9 knockout screens. *Genome Biol.* *15*, 554.
- Li, Y., Wang, Z., Ajani, J.A., and Song, S. (2021). Drug resistance and Cancer stem cells. *Cell Commun. Signal.* *19*, 19.
- Love, M.I., Huber, W., and Anders, S. (2014). Moderated estimation of fold change and dispersion for RNA-seq data with DESeq2. *Genome Biol.* *15*, 550.
- Matulay, J.T., Woldu, S.L., Lim, A., Narayan, V.M., Li, G., Kamat, A.M., and Anderson, C.B. (2019). The impact of squamous histology on survival in patients with muscle-invasive bladder cancer. *Urol. Oncol.* *37*, 353.e17–353.e24.
- Medema, J.P. (2013). Cancer stem cells: the challenges ahead. *Nat. Cell Biol.* *15*, 338–344.
- Mitoma, H., Horiuchi, T., Tsukamoto, H., and Ueda, N. (2018). Molecular mechanisms of action of anti-TNF-alpha agents - comparison among therapeutic TNF-alpha antagonists. *Cytokine* *101*, 56–63.
- Mu, P., Zhang, Z., Benelli, M., Karthaus, W.R., Hoover, E., Chen, C.C., Wongvipat, J., Ku, S.Y., Gao, D., Cao, Z., et al. (2017). SOX2 promotes lineage plasticity and antiandrogen resistance in TP53- and RB1-deficient prostate cancer. *Science* *355*, 84–88.
- Na, F., Pan, X., Chen, J., Chen, X., Wang, M., Chi, P., You, L., Zhang, L., Zhong, A., Zhao, L., et al. (2022). KMT2C deficiency promotes small cell lung cancer metastasis through DNMT3A-mediated epigenetic reprogramming. *Nat. Cancer* *3*, 753–767.
- Nestorowa, S., Hamey, F.K., Pijuan Sala, B., Diamanti, E., Shepherd, M., Laurenti, E., Wilson, N.K., Kent, D.G., and Göttgens, B. (2016). A single-cell resolution map of mouse hematopoietic stem and progenitor cell differentiation. *Blood* *128*, e20–31.
- Olson, O.C., and Joyce, J.A. (2015). Cysteine cathepsin proteases: regulators of cancer progression and therapeutic response. *Nat. Rev. Cancer* *15*, 712–729.
- Orning, P., Weng, D., Starheim, K., Ratner, D., Best, Z., Lee, B., Brooks, A., Xia, S., Wu, H., Kelliher, M.A., et al. (2018). Pathogen blockade of TAK1 triggers caspase-8-dependent cleavage of gasdermin D and cell death. *Science* *362*, 1064–1069.
- Oser, M.G., Niederst, M.J., Sequist, L.V., and Engelman, J.A. (2015). Transformation from non-small-cell lung cancer to small-cell lung cancer: molecular drivers and cells of origin. *Lancet Oncol.* *16*, e165–172.
- Otto, H.H., and Schirmeister, T. (1997). Cysteine proteases and their inhibitors. *Chem. Rev.* *97*, 133–172.
- Palermo, C., and Joyce, J.A. (2008). Cysteine cathepsin proteases as pharmacological targets in cancer. *Trends Pharmacol. Sci.* *29*, 22–28.
- Pan, X., Wang, J., Guo, L., Na, F., Du, J., Chen, X., Zhong, A., Zhao, L., Zhang, L., Zhang, M., et al. (2022). Identifying a confused cell identity for esophageal squamous cell carcinoma. *Signal Transduct. Target. Ther.* *7*, 122.

- Park, S., Rong, L., Owczarek, T.B., Bernardo, M.D., Shoulson, R.L., Chua, C.W., Kim, J.Y., Lankarani, A., Chakrapani, P., Syed, T., et al. (2021). Novel mouse models of bladder cancer identify a prognostic signature associated with risk of disease progression. *Cancer Res.* **81**, 5161–5175.
- Pierce, G.B., and Wallace, C. (1971). Differentiation of malignant to benign cells. *Cancer Res.* **31**, 127–134.
- Platt, R.J., Chen, S., Zhou, Y., Yim, M.J., Swiech, L., Kempton, H.R., Dahlman, J.E., Parnas, O., Eisenhaure, T.M., Jovanovic, M., et al. (2014). CRISPR-Cas9 knockin mice for genome editing and cancer modeling. *Cell* **159**, 440–455.
- Puzio-Kuter, A.M., Castillo-Martin, M., Kinkade, C.W., Wang, X., Shen, T.H., Matos, T., Shen, M.M., Cordon-Cardo, C., and Abate-Shen, C. (2009). Inactivation of p53 and Pten promotes invasive bladder cancer. *Genes Dev.* **23**, 675–680.
- Quintana, E., Shackleton, M., Foster, H.R., Fullen, D.R., Sabel, M.S., Johnson, T.M., and Morrison, S.J. (2010). Phenotypic heterogeneity among tumorigenic melanoma cells from patients that is reversible and not hierarchically organized. *Cancer Cell* **18**, 510–523.
- Quintanal-Villalonga, Á., Chan, J.M., Yu, H.A., Pe'er, D., Sawyers, C.L., Sen, T., and Rudin, C.M. (2020). Lineage plasticity in cancer: a shared pathway of therapeutic resistance. *Nat. Rev. Clin. Oncol.* **17**, 360–371.
- Ramírez, F., Ryan, D.P., Grüning, B., Bhardwaj, V., Kilpert, F., Richter, A.S., Heyne, S., Dündar, F., and Manke, T. (2016). deepTools2: a next generation web server for deep-sequencing data analysis. *Nucleic Acids Res.* **44**, W160–W165.
- Robertson, A.G., Kim, J., Al-Ahmadie, H., Bellmunt, J., Guo, G., Cherniack, A.D., Hinoue, T., Laird, P.W., Hoadley, K.A., Akbani, R., et al. (2017). Comprehensive molecular characterization of muscle-invasive bladder cancer. *Cell* **171**, 540–556.e25.
- Roupret, M., Babjuk, M., Compérat, E., Zigeuner, R., Sylvester, R.J., Burger, M., Cowan, N.C., Gontero, P., Van Rhijn, B.W.G., Mostafid, A.H., et al. (2018). European association of urology guidelines on upper urinary tract urothelial carcinoma: 2017 update. *Eur. Urol.* **73**, 111–122.
- Ruan, J.L., Hsu, J.W., Browning, R.J., Stride, E., Yildiz, Y.O., Vojnovic, B., and Kiltie, A.E. (2019). Mouse models of muscle-invasive bladder cancer: key considerations for clinical translation based on molecular subtypes. *Eur. Urol. Oncol.* **2**, 239–247.
- Said, J.W., Nash, G., Sassoon, A.F., Shintaku, I.P., and Banks-Schlegel, S. (1983). Involucrin in lung tumors. A specific marker for squamous differentiation. *Lab. Invest.* **49**, 563–568.
- Sequist, L.V., Waltman, B.A., Dias-Santagata, D., Digumarthy, S., Turke, A.B., Fidias, P., Bergtholm, K., Shaw, A.T., Gettinger, S., Cosper, A.K., et al. (2011). Genotypic and histological evolution of lung cancers acquiring resistance to EGFR inhibitors. *Sci. Transl. Med.* **3**, 75ra26.
- Sfakianos, J.P., Daza, J., Hu, Y., Anastos, H., Bryant, G., Bareja, R., Badani, K.K., Galsky, M.D., Elemento, O., Faltas, B.M., and Mulholland, D.J. (2020). Epithelial plasticity can generate multi-lineage phenotypes in human and murine bladder cancers. *Nat. Commun.* **11**, 2540.
- Sjödahl, G., Lauss, M., Lövgren, K., Chebil, G., Gudjonsson, S., Veerla, S., Patschan, O., Aine, M., Fernö, M., Ringnér, M., et al. (2012). A molecular taxonomy for urothelial carcinoma. *Clin. Cancer Res.* **18**, 3377–3386.
- Staack, A., Tolic, D., Kristiansen, G., Schnorr, D., Loening, S.A., and Jung, K. (2004). Expression of cathepsins B, H, and L and their inhibitors as markers of transitional cell carcinoma of the bladder. *Urology* **63**, 1089–1094.
- Street, K., Rizzo, D., Fletcher, R.B., Das, D., Ngai, J., Yosef, N., Purdom, E., and Dudoit, S. (2018). Slingshot: cell lineage and pseudotime inference for single-cell transcriptomics. *BMC Genom.* **19**, 477.
- Stuart, T., Butler, A., Hoffman, P., Hafemeister, C., Papalexi, E., Mauck, W.M., 3rd, Hao, Y., Stoeckius, M., Smibert, P., and Satija, R. (2019). Comprehensive integration of single-cell data. *Cell* **177**, 1888–1902.e21.
- Sui, H., Shi, C., Yan, Z., and Wu, M. (2016). Overexpression of Cathepsin L is associated with chemoresistance and invasion of epithelial ovarian cancer. *Oncotarget* **7**, 45995–46001.
- Tarbell, E.D., and Liu, T. (2019). HMMRATAC: a hidden Markov ModelER for ATAC-seq. *Nucleic Acids Res.* **47**, e91.
- Tran, L., Xiao, J.F., Agarwal, N., Duex, J.E., and Theodorescu, D. (2021). Advances in bladder cancer biology and therapy. *Nat. Rev. Cancer* **21**, 104–121.
- Valent, P., Bonnet, D., De Maria, R., Lapidot, T., Copland, M., Melo, J.V., Chomienne, C., Ishikawa, F., Schuringa, J.J., Stassi, G., et al. (2012). Cancer stem cell definitions and terminology: the devil is in the details. *Nat. Rev. Cancer* **12**, 767–775.
- Vasan, N., Baselga, J., and Hyman, D.M. (2019). A view on drug resistance in cancer. *Nature* **575**, 299–309.
- Waddington, C.H. (1957). *The Strategy of the Genes; a Discussion of Some Aspects of Theoretical Biology* (London: Allen & Unwin).
- Walts, A.E., Said, J.W., Siegel, M.B., and Banks-Schlegel, S. (1985). Involucrin, a marker of squamous and urothelial differentiation. An immunohistochemical study on its distribution in normal and neoplastic tissues. *J. Pathol.* **145**, 329–340.
- Xiao, Y., Cong, M., Li, J., He, D., Wu, Q., Tian, P., Wang, Y., Yang, S., Liang, C., Liang, Y., et al. (2021). Cathepsin C promotes breast cancer lung metastasis by modulating neutrophil infiltration and neutrophil extracellular trap formation. *Cancer Cell* **39**, 423–437.e7.
- Yang, G., Bondaruk, J., Cogdell, D., Wang, Z., Lee, S., Lee, J.G., Zhang, S., Choi, W., Wang, Y., Liang, Y., et al. (2020). Urothelial-to-Neural plasticity drives progression to small cell bladder cancer. *iScience* **23**, 101201.
- Yu, G., Wang, L.G., and He, Q.Y. (2015). ChIPseeker: an R/Bioconductor package for ChIP peak annotation, comparison and visualization. *Bioinformatics* **31**, 2382–2383.
- Yu, P., Zhang, X., Liu, N., Tang, L., Peng, C., and Chen, X. (2021). Pyroptosis: mechanisms and diseases. *Signal Transduct. Target. Ther.* **6**, 128.
- Zheng, X., Chou, P.M., Mirkin, B.L., and Rebbaa, A. (2004). Senescence-initiated reversal of drug resistance: specific role of cathepsin L. *Cancer Res.* **64**, 1773–1780.
- Zou, M., Toivanen, R., Mitrofanova, A., Floch, N., Hayati, S., Sun, Y., Le Magnen, C., Chester, D., Mostaghel, E.A., Califano, A., et al. (2017). Transdifferentiation as a mechanism of treatment resistance in a mouse model of castration-resistant prostate cancer. *Cancer Discov.* **7**, 736–749.

STAR★METHODS

KEY RESOURCES TABLE

REAGENT or RESOURCE	SOURCE	IDENTIFIER
Antibodies		
Recombinant Anti-p40 - DeltaNp63 antibody [EPR17863-47]	Abcam	Cat# ab203826
Anti-Cytokeratin 14 antibody [LL002]	Abcam	Cat# ab7800; RRID:AB_306091
Anti-EpCAM antibody	Abcam	Cat# ab71916; RRID:AB_1603782
Recombinant Anti-Ki67 antibody [SP6]	Abcam	Cat# ab16667; RRID:AB_30245
Cytokeratin 5 Monoclonal Antibody (2C2)	Thermo Fisher Scientific	Cat# MA5-17057; RRID:AB_2538529
THE™ beta Actin Antibody [HRP], mAb, Mouse	Genscript	Cat# A00730; RRID:AB_914100
Cathepsin H (F-7)	Santa Cruz	Cat# sc-398527
GSDMC Rabbit pAb	ABclonal	Cat# A14550; RRID:AB_2769694
Caspase-8 (4C2) Mouse mAb	ZEN BIO	Cat# 250106
TNF alpha Rabbit pAb	ZEN BIO	Cat# 251341
Anti-involucrin Antibody (A-5)	Santa Cruz	Cat# sc-398952
Anti-Keratin 16 Rabbit mAb (JRM-10024-42H5L1)	PTM BIO	Cat# PTM-5341
APC Rat Anti-Mouse CD326	BD Pharmingen	Cat# 563478; RRID:AB_2738234
FITC anti-human CD326 (EpCAM) Antibody	BioLegend	Cat# 324204; RRID:AB_756078
PE anti-human CD298 Antibody	BioLegend	Cat# 341704; RRID:AB_2274458
APC anti-human CD45 Antibody	BioLegend	Cat# 304037; RRID:AB_2562049
Recombinant Mouse TNF- α	BioLegend	Cat# 575202
Infliximab (anti-TNF-alpha)	Selleck	Cat# A2019
Bacterial and virus strains		
DH5 α	TsingKe	TSV-A07
Biological samples		
Mouse sample	This manuscript	N/A
Human bladder samples	West China Hospital	Table S3
Chemicals, peptides, and recombinant proteins		
DMED/F12	Gibco	REF# C11330500BT
DMEM	Gibco	REF# C11995500BT
Penicillin/Streptomycin	Gibco	REF# 15140-122
GlutaMAX	Gibco	REF# 35050-061
B27	Gibco	Cat# A3582801
N ₂	Gibco	Cat# 17502048
N-acetylcysteine	Sigma	A9165
Nicotinamide	Sigma	N0636
Mouse recombinant epidermal growth factor	Peprtech	AF-100-15-1000
Mouse recombinant Noggin	Peprtech	120-10C-250
Mouse recombinant FGF10	Peprtech	100-26-1000
R-spondin-1	Peprtech	120-38-1000
A83-01	Peprtech	Cat# 9094360
TrypLE	Gibco	REF# 12605-028
T7E1	Vazyme	Cat# EN303-01
Protein kinase K	Solarbio	P9460

(Continued on next page)

Continued		
REAGENT or RESOURCE	SOURCE	IDENTIFIER
D-luciferin potassium salt	Biovision	Cat# 7903-10PK
Gemcitabine	Selleck	Cat# S1714
Cisplatin	Selleck	Cat# S1166
E-64	Selleck	Cat# S7379
Matrigel	Corning	Cat# 356237
TRIzol	Applied Biosystems	REF# 15596026
Collagenase I	Gibco	REF# 17100-017
Collagenase IV	Gibco	REF# 17104-019
M-MLV Reverse Transcriptase	Invitrogen	Cat# 28025013
SYBR	Applied Biosystems	Cat# A25741
DMSO	MPbio	Cat# 196055
DPBS	Gibco	REF# C14190500BT
Fetal bovine serum	WISENT	Cat# 086-150
Trypsin	Gibco	REF# 25200-072
Cell Counting Kit-8	MCE	HY-K0301
RIPA buffer	Beyotime	Cat# P0013
Protease inhibitors	Beyotime	Cat# P1045
Critical commercial assays		
Chromium™ Single Cell 3' Library & Gel Bead Kit v2	10x Genomics	Cat# PN-120237
Chromium™ Single Cell A Chip Kit	10x Genomics	Cat# PN-120236
Chromium™ i7 Multiplex Kit	10x Genomics	Cat# PN-120262
Deposited data		
Western Blot source data	Mendeley	https://doi.org/10.17632/y3h46d6wzn.1
Data files for Omics data (raw data of ATAC-seq, RNA-seq, scRNA-seq)	This manuscript	GEO: GSE192575
TCGA BLCA data	TCGA	https://www.cbioportal.org/study/summary?id=blca_tcga_pub_2017
Experimental models: Cell lines		
Mouse: TPM naïve Cells	This manuscript	N/A
Mouse: Chemoresistant Cells	This manuscript	N/A
Human PDXs: human bladder cancer fresh tumor tissues	West China Hospital	Table S3
Human: HEK-293T	ATCC	Cat# CRL-1573
Experimental models: Organisms/strains		
Mouse:sg <i>Trp53</i> ; sg <i>Pten</i> ;Myc-Luci2;	This manuscript	N/A
Mouse:CAG-Cas9-EGFP	Jackson Lab	https://www.jax.org/jax-mice-and-services
Mouse: C57BL/6	Jackson Lab	Cat# 000664
Mouse: BALB/c Nude	Beijing HFK Bioscience	Cat# 13001A
Mouse: NCG	GemPharmatech	Cat# T001475
Oligonucleotides		
CRISPR sgRNAs	Zhang Lab;MIT	Table S7; http://crispr.mit.edu/
RT-qPCR primer	MGH CCIB	Table S7; https://pga.mgh.harvard.edu/primerbank/index.html
Recombinant DNA		
V2TC-sgRNA	This manuscript	N/A
V2TC-EPCAM ^{pro} -mCherry	This manuscript	N/A
PIL-Myc-Luci2	This manuscript	N/A

(Continued on next page)

Continued

REAGENT or RESOURCE	SOURCE	IDENTIFIER
Software and algorithms		
Code generated for this study	This manuscript	https://github.com/Xuelan-Chen/bladder_chemoresistant
Bowtie2	(Langmead and Salzberg, 2012)	http://bowtie-bio.sourceforge.net/bowtie2/index.shtml
Cellranger (v.3.0.0)	10x Genomics	https://support.10xgenomics.com/single-cell-gene-expression/software
ChIPseeker	(Yu et al., 2015)	https://www.bioconductor.org/packages/release/bioc/html/ChIPseeker.html
deepTools	(Ramirez et al., 2016)	https://deeptools.readthedocs.io/en/develop/
DESeq2	(Love et al., 2014)	https://bioconductor.org/packages/release/bioc/html/DESeq2.html
GATK (v4.1.3)	Broad Institute	https://gatk.broadinstitute.org/hc/en-us
ggplot2	bioconductor	https://cran.r-project.org/package=ggplot2
Ggpubr	CRAN	https://rpkgs.datanovia.com/ggpubr/
HMMRATAC	(Tarbell and Liu, 2019)	https://github.com/LiuLabUB/HMMRATAC
MAGeCK	(Li et al., 2014)	https://sourceforge.net/p/mageck/wiki/Home/
Monocle3	(Cao et al., 2019)	https://cole-trapnell-lab.github.io/monocle3
NGmerge	(Gaspar, 2018)	https://github.com/jsh58/NGmerge
Samtools	(Li et al., 2009)	https://github.com/samtools/samtools
Seurat (v3)	(Stuart et al., 2019)	https://satijalab.org/seurat/
Slingshot	(Street et al., 2018)	https://github.com/kstreet13/slingshot
STAR	(Dobin et al., 2013)	https://github.com/alexdobin/STAR
ImageJ	ImageJ	https://imagej.nih.gov/ij/
Snapgene	Snapgene	https://www.snapgene.com
Graphpad Prism 8	Graphpad Software	www.graphpad.com/scientific-software/prism/
FlowJo v10	FlowJo LLC	www.flowjo.com

RESOURCE AVAILABILITY**Lead contact**

Correspondence and requests regarding this manuscript should be sent to and will be fulfilled by the lead investigator Chong Chen (chongchen@scu.edu.cn).

Materials availability

All unique reagents generated in this study are available from the [lead contact](#) with a completed Materials Transfer Agreement.

Data and code availability

- The RNA-seq, ATAC-seq and scRNA-seq data in this study are deposited in NCBI GEO: [GSE192575](https://www.ncbi.nlm.nih.gov/geo/query/acc.cgi?acc=GSE192575). TCGA BLCA dataset is download from https://www.cbiportal.org/study/summary?id=blca_tcga_pub_2017. The original western blot source data are deposited in Mendeley: <https://doi.org/10.17632/y3h46d6wzn.1>. Accession number and links are listed in the [key resources table](#).
- The original code has been deposited at GitHub at https://github.com/Xuelan-Chen/bladder_chemoresistant, and link can be found in the [key resources table](#).
- Any additional information required to reanalyze the data reported in this work paper is available from the [lead contact](#) upon request.

EXPERIMENTAL MODEL AND SUBJECT DETAILS

Human specimens

This study was approved by the Ethical Research Committee of the West China Hospital (2019-933/2020-330). Written informed consent was signed by patients for providing tissues for research and genomic profiling. Written informed consent was not required for patients who were involved in retrospective analysis. All patients were pathologically confirmed to have MIBC by pathologists in West China Hospital. In cases treated with neoadjuvant chemotherapy, T stages before chemotherapy were evaluated based on radiologic and pathological assessments by the investigator, and the post-chemotherapy T stages were assessed by pathological diagnosis. All sample collection procedures complied with the regular routine in clinical practice. Fresh tumor tissues were collected immediately after surgery in cold preservation medium and delivered to the lab for further analyses and culturing. The characters and related applications of clinical patients included in this study are shown in [Table S3](#).

Mice

Mice were kept in the specific pathogen-free animal facility at Sichuan University with autoclaved food, bedding and water. Animals were housed at room temperature ($23 \pm 2^\circ\text{C}$) at a humidity of 30–70% on a 12-h light/12-h dark cycle (6:00–18:00). All animal procedures were approved by the Animal Care and Use Committee of Sichuan University (No. 20181204027). C57BL/6 (Jackson Lab, Cat# 000664) and CAG-Cas9-EGFP mice (Cat# JAX:026179, RRID: IMSR_JAX:026179) (Male, 8–10 weeks and ~ 20 g weight), BALB/cA-nu mice (Beijing HFK Bioscience, Cat# 13001A) and NCG (GemPharmatech, RRID:SCR_017239) (Male, 6–8 weeks and ~ 20 g weight) were purchased from the indicated providers. Mice were monitored for tumorigenesis by bioluminescent imaging and magnetic resonance image scan.

Cell culture

HEK 293T cells (CRL-1573) were from ATCC and cultured at 37°C with 5% CO_2 in DMEM supplemented with 10% (vol/vol) fetal bovine serum (WISENT, Cat#086-150) and penicillin (100 U ml^{-1})/streptomycin (0.1 mg ml^{-1}). The HEK 293T cell line was routinely tested for Mycoplasma by PCR. Experiments were performed within 4 weeks after fresh viable cells were thawed.

METHOD DETAILS

Organoid culture

Mouse normal bladder or tumors were cut into 5 mm^3 cubes and the isolated tissues were incubated in DMEM/F12 buffer containing 1 mg/mL Collagenase I (GIBCO, Cat# 17100-017) and 0.5 mg/mL Collagenase IV (GIBCO, Cat# 17104-019) for one hour at 37°C , mechanical pipetting every 15 minutes, followed by filtration through $100 \mu\text{m}$ cell strainers. After lysing red blood cells in ammonium-chloride-potassium (ACK) lysis buffer, cells were collected by centrifugation and resuspended in ice-cold Matrigel (Corning, Cat# 356237); the mixture was plated into a 48-well tissue culture plate ($40 \mu\text{L}$ drop with 10,000 cells) and incubated for 15 min at 37°C . Pre-warmed organoid culture medium was then added. The recipe of bladder organoid medium was: DMEM/F12 was supplemented with penicillin/streptomycin (GIBCO, Cat# 15140-122), 2 mM GlutaMAX (Peprotech, Cat# 35050-061), $1 \times$ B27 (GIBCO, Cat# A3582801), $1 \times$ N2 (GIBCO, Cat# 17502048), 1 mM N-acetylcysteine (Sigma, Cat# A9165) and 10mM Nicotinamide (Sigma, Cat# N0636), 100 ng/mL mouse recombinant FGF10 (Peprotech, Cat# 100-26-1000), 50 ng/mL mouse recombinant EGF (Peprotech, Cat# AF-100-15-1000), 500 nM A83-01 (Peprotech, Cat# 9094360), 100 ng/mL mouse recombinant Noggin (Peprotech, Cat# 120-10C-250), 125 ng/mL R-spondin-1 (Peprotech, Cat# 120-38-1000), 10% Wnt-3A conditioned medium.

For organoid passaging, bladder organoids were released in TrypLE™ (GIBCO, Cat# 12605-028), and mechanical dissociation was performed every 5 minutes at 37°C , followed by centrifugation at 1,500 rpm for 5 minutes. Ultimately, single cells were reseeded in Matrigel and cultured as described above. The organoid medium was refreshed every 2–3 d.

Organoid genome editing

sgRNAs designed on the CRISPR Design Tool (<http://crispr.mit.edu/>) were cloned into the lentiviral vector V2TC which expressed sgRNA and mCherry, sgRNA sequences were listed in [Table S7](#). Organoids were dissociated using TrypLE™ (Gibco, 12605-028) and cells were mixed with lentivirus and centrifuged for 1 hr at 2,000 rpm, and then incubated for 1.5 hr at 37°C , finally resuspended with ice-cold Matrigel. Mutation validation was performed by the T7E1 (Vazyme, Cat# EN303-01) assay.

Human MIBC sample processing

Fresh tumor tissues derived from MIBC patients or PDX mice were washed with PBS 3 times and cut into 5 mm^3 cubes. After the tissue preparation, 1 mg/mL Collagenase I (GIBCO, Cat# 17100-017) and 0.5 mg/mL Collagenase IV (GIBCO, Cat# 17104-019) were used to digest the samples for 2 hours at 37°C , followed by centrifugation at $400 \times g$ for 6 minutes. After discarding the supernatant, 10 mL Trypsin-EDTA (Gibco, Cat# 25200072) was added for further dissociation at 37°C for 15 min. DMEM/F12 (GIBCO, Cat# C11330500BT) containing 10% fetal bovine serum (WISENT, Cat# 086-150) was added to stop the digestion and cell suspension was filtered using $100 \mu\text{m}$ strainers and spun at $300 \times g$ for 5 min at room temperature. After lysing red blood cells in ACK lysis buffer, 5mL 0.04% BSA-PBS was used to wash cells. Finally, cells were collected for single-cell RNA-seq or transplantation.

Mouse models establishment

The primary orthotopic MIBC model was generated by injecting mouse normal bladder organoids with *Trp53* and *Pten* mutation as well as *Myc* amplification (TPM) into the bladder. Gene edited organoids were digested with TrypLE™ at 37°C for 10 minutes and spun at 400×g for 5 min at room temperature. The collected cells were resuspended with 50% Matrigel mixed with PBS. Organoid suspension was injected into the bladder wall of BALB/c Nude mice (male, 6–8 weeks) using 29-gauge insulin syringe after anesthesia induction.

For chemosensitive or resistant MIBC model establishment, TPM tumor cells (5×10^3 cells per mouse) were orthotopically transplanted into mouse bladder as described above. Mice were left for at least 5 days for tumor development. After tumor volume was measured by living image, mice were allocated into two groups for weekly vehicle or gemcitabine and cisplatin (GC) treatment. Tumor cells from the vehicle or chemotherapy treated bladder tumors were second-transplanted into new mice respectively (5×10^3 cells per mouse) and their response to chemotherapy were evaluated by weekly Bioluminescence Imaging, and all recipient mice were sacrificed after 7 rounds of GC treatment.

For PDX model establishment, fresh tumor tissues were minced into pieces and subcutaneously transplanted into NCG mice (male, 6–8 weeks). Generally, successfully established PDX models could be used for research after 3 passages. For PDX models originated from different patients, their response to GC treatment was evaluated at first; the clinical information of all PDX models we used was listed in Table S3.

In vitro treatment

For *in vitro* chemotherapy, mouse chemosensitive or chemoresistant tumor organoids were dissociated in TrypLE™ and seeded into 96-well plates (4000 cells per well). After 72 h culturing, organoids were treated with 0, 5, 10, 20, 40, 80 μ M cisplatin (three replicate wells/concentration). The viability of organoids was quantified using Cell Counting Kit-8 (CCK-8) after 72 h treatment and the viability of treated organoids was calculated by normalizing to vehicle group. For E64 treatment, organoids were treated with 0, 0.45, 1.35, 4.05, 12.15, 25 mM E64 for 72 h. The viability of organoids was quantified using CCK-8 (MCE, HY-K0301) after treatment. In terms of TNF α treatment, mouse chemoresistant tumor organoids were treated with 0, 4, 20, 100, 500 ng/mL recombinant mouse TNF α (BioLegend, Cat# 575202) for 72 h. CCK-8 was used to quantify the viability of organoids.

In vivo treatment

When xenograft tumors reached a palpable size, the recipient mice were allocated into different treatment groups: Vehicle control (0.9% saline); GC treatment group; E64 treatment group; E64 plus Infliximab (anti-TNF α) treatment group. For systematic administration of GC treatment, mice were weekly treated with 50 mg/kg gemcitabine (Selleck, Cat# S1149) on day 1 and sequential 3 mg/kg cisplatin (Selleck, Cat# S1166) on day 2 by intraperitoneal injection. In E64 treatment experiments, mice were pretreated with only a single dose of GC and followed by vehicle or 20 mg/kg E64 (Selleck, Cat# S7379) daily treatment for 14 days. For E64 plus Infliximab (anti-TNF α) treatment, chemoresistant PDX mice were pretreated with only a single dose of GC, and Infliximab (10 mg/kg; Selleck, Cat# A2019) was given via intraperitoneal injection on day 1, 5, 9, 13 and 20 mg/kg E64 was daily given via intraperitoneal injection for 14 days. Tumor volumes were measured every 7 days by Bioluminescence Imaging in orthotopic MIBC mouse models or every 3 days by caliper in subcutaneous models. Mice were sacrificed and analyzed at the indicated time points.

MRI imaging and bioluminescent imaging

MRI imaging of the bladder was performed by a clinical Siemens 3.0 T MRI scanner equipped with a mouse coil. The conventional T2 weighted (T2WI) FSE sequence was TR/TE = 3000 ms/93 ms, slice thickness = 1 mm, slices = 15, Fov = 66 mm \times 66 mm and voxel size = 0.2 \times 0.2 \times 1.0 mm³.

For bioluminescent imaging, mice were given 250 μ L (150 mg/kg) D-luciferin potassium salt (Biovision, Cat# 7903-10PK) intraperitoneally and imaged on the IVIS Spectrum *In Vivo* Imaging System (PerkinElmer).

RNA extraction and RT-qPCR

Total RNA extraction using TRIzol reagent (Applied Biosystems, Cat# 15596026) and complementary DNA (cDNA) synthesization using M-MLV Reverse Transcriptase (Invitrogen, Cat# 28025013) were performed under the manufacturer's instructions. RT-qPCR was performed using Powerup SYBR Green master mix (Applied Biosystems, A25741) in QuantStudio 3 (Applied Biosystems), all primers for RT-qPCR were listed in Table S7.

Antibodies and reagents

Antibodies of Anti-p40-deltaNp63 (Abcam Cat# ab203826), anti-Cytokeratin 14 (Abcam Cat# ab7800, RRID:AB_306091), anti-EP-CAM (Abcam Cat# ab71916, RRID:AB_1603782), anti-Ki-67 (Abcam Cat# ab16667, RRID:AB_302459) were from Abcam; anti-CK5 (Thermo Fisher Scientific Cat# MA5-17057, RRID:AB_2538529) was from Thermo Fisher; anti- β -Actin was from Genscript (GenScript Cat# A00730, RRID:AB_914100); anti-Cathepsin H (F-7) and anti-involucrin antibody (A-5) were from Santa Cruz; anti-GSDMC was from Abclonal (Abclonal Cat# A14550, RRID: AB_2769694); anti-Caspase-8 (4C2) (ZEN BIO Cat# 250106) and anti-TNF alpha (ZEN BIO Cat# 251341) antibodies were from ZEN BIO; anti-TNFR1 (Proteintech Cat# 21574-1-AP, RRID:AB_10734433) was from Proteintech; anti-Keratin 16 antibody (PTM BIO Cat# PTM-5341) was from PTM BIO; APC Rat Anti-Mouse CD326 (BD Cat# 563478) was from BD Pharmingen; FITC anti-human CD326 (EPCAM) antibody (BioLegend Cat# 324204, RRID: AB_756078), PE

anti-human CD298 antibody (BioLegend Cat# 41704, RRID: AB_2274458) and APC anti-human CD45 antibody (BioLegend Cat# 304037, RRID: AB_2562049) were purchased from BioLegend.

Western blotting

Whole cell and tissue lysates were extracted in RIPA buffer (Beyotime, Cat# P0013) supplemented with protease inhibitors (Beyotime, Cat# P1045), followed by SDS-PAGE gel electrophoresis and blotting onto PVDF membranes. Primary antibodies were applied at 1:1000-1:5000 dilution in 5% non-fatty milk or BSA in TBST and incubated overnight at 4°C. HRP-conjugated secondary antibodies were applied at 1:10000 dilution. Images were developed by NcmECL Ultra Reagent (NCM biotech).

H&E, immunohistochemistry and immunofluorescence

Tumor sections of 5 μm thickness were cut from tumor tissues fixed by 4% paraformaldehyde. H&E staining was performed according to the standard protocol using hematoxylin and eosin. In terms of immunohistochemistry (IHC) and immunofluorescence (IF) staining, primary antibodies were applied at 1:50-1:500 dilution in 2% goat serum and incubated overnight at 4°C. A two-step detection kit (PV-9001 and PV-9002) was used for IHC, and hematoxylin for nuclear staining. As for IF, fluorescence-conjugated secondary antibodies were used.

Squamous score evaluation

To evaluate the squamous score of mice and human chemosensitive tumors with different rounds of chemotherapy, the IHC stainings of p40 and CK5 were performed, and their positive percentages were independently scored by ImageJ (Version 1.53a, RRID:SCR_003070). The total squamous scores were 100 points and each marker accounts for 50%.

Keratin pearl area evaluation

To quantify the keratin pearls area of each tumor, the scanned H&E slices were analyzed by CaseViewer (Version 2.4). At least 3 independent areas were chosen from each slide and the area of keratin pearls was manually outlined and automatically calculated.

Flow cytometry

Surface antigen detection by FACS (BD, FACSAriaIII) was carried out to isolate T1 and T2 tumor cells from mouse chemosensitive and chemoresistant TPM and human PDX tumors by surface marker EPCAM. Cells dissociated from tumors as described above were stained for 30 min and washed twice with PBS containing 2% FBS. After staining prepared, T1 and T2 tumor cells sorting was performed on FACSAriaIII (BD) and sorted T1 and T2 cells (1×10^4 cells per mouse) were orthotopically or subcutaneously transplanted into mouse to evaluate their growth and response to chemotherapy *in vivo*.

Protein and peptide processing for mass spectrometry (MS)

Tumor tissue lysates were prepared by RIPA lysis buffer (same as western blotting) containing 20mM Tris (pH 7.5) (Beyotime, Cat# P0013). Samples were incubated in ice for 30 min and then briefly sonicated for 2 mins. The protein concentration was determined with BCA kit. The protein samples were precipitated at -20°C for 2 h and redissolved in 200 mM TEAB and ultrasonically dispersed. Trypsin was added at 1:50 trypsin-to-protein mass ratio for digestion overnight. The tryptic peptides desalted with Strata X C18 SPE column (Phenomenex) and dried by vacuum centrifugation. The TMT/TMTpro reagent (TMT10plex™ Isobaric Mass Tagging Kit, Thermo Scientific, Cat# 90113) was used for labeling based on manufacturer's protocol. The sample was fractionated into fractions by high pH reverse-phase HPLC using Agilent 300 Extend C18 column. For LC-MS/MS analysis, the resulting peptides were analyzed in Q Exactive HF-X Hybrid Quadrupole-Orbitrap MS System (Thermo Scientific) with a nano-electrospray ion source.

Living image tracking

To clarify the acquired chemoresistance by lineage plasticity, we designed an *EPCAM*-promoter-mCherry reporter assay. 700bp fragments before *EPCAM* genomic transcription start site 'ATG' were selected as the promoter. Promoter fragments were amplified by PCR and then cloned into the lentiviral vector V2TC using XbaI and KpnI sites with homologous recombination. To perform the living image tracking on the chemosensitive tumor cells, the V2TC-*EPCAM*-promoter vector was packaged as lentivirus and infected human chemosensitive MIBC organoids as described above. After 72 h, the culture medium was replaced with fresh organoid medium containing 1 μM cisplatin and cells were traced for detection of red fluorescence by fluorescence microscope (OLYMPUS IX-71) for 48 h.

Bar-code-based lineage tracing

The mouse chemosensitive tumor cells were transduced with a barcoding library with 33219 barcodes of 20bp length in a lentiviral construct and then orthotopically transplanted into recipient mice as described above. One week after transplantation, the recipient mice received two rounds of GC treatment and then sacrificed to purify the T1 and T2 cells with anti-EPCAM antibodies using Flow cytometry. The genome DNA of sorted T1 and T2 cells were extracted and followed by barcode libraries construction with PCR, which was sequenced by Next Generation Sequencing. The PCR-amplified libraries were analyzed by MAGeCK (Li et al., 2014).

RNA-seq analyses

RNA-seq libraries were constructed by Illumina Stranded mRNA Sample Preparation Kit (NEB, Cat# E7770) according to the manufacturer's protocol, and were sequenced by Illumina NovaSeq 6000 sequencing machine with 150-bp paired-end reads. The RNA-seq reads were aligned to the mouse reference genome (GRCm38) or human reference genome (hg19) by STAR_2.6.0a (Dobin et al., 2013). Transcript abundance was normalized and measured by Transcripts Per Kilobase Million (TPM). DESeq2 (Love et al., 2014) (RRID:SCR_015687) was used to identify differential expression genes. Genes with an absolute fold change greater than 0.5 and p-value < 0.05 were counted as differentially expressed genes. Pheatmap (RRID:SCR_016418) was used to display heatmaps of the expression levels of differentially expressed genes, which normalized by z-score. To identify functional categories of differentially expressed genes, Gene Ontology and KEGG enrichment analyses (RRID:SCR_012773) were performed using the R package clusterProfiler (RRID:SCR_016884). The TPM data were used for GSEA (RRID:SCR_003199).

ATAC-seq analyses

Library preparation was performed as previously described (Buenrostro et al., 2013). The library was sequenced by Illumina NovaSeq 6000 sequencing machine with 150-bp paired-end reads. NGmerge (Gaspar, 2018) was used to remove the adapters in raw data. Bowtie2 (v2.2.1) (Langmead and Salzberg, 2012) (RRID:SCR_016368) was used to align the reads with the mm10 genome. Samtools (Li et al., 2009) (RRID:SCR_002105) was used to generate the .bam files. MarkDuplicates, implemented in GATK (v4.1.3) (RRID:SCR_001876) was used with -REMOVE_DUPLICATES = true to remove the PCR duplicates. Bigwig files were generated by bamCoverage with bins per million (BPM) normalizing to remove library sizes' effects. For optimizing peaks calling in ATAC-seq data, HMMRATAC (Tarbell and Liu, 2019) was used as the peak detectors to call peaks region in each sample. The heatmap and average profile of ATAC-seq peaks were generated with deepTools (Ramírez et al., 2016) (RRID:SCR_016366). ChIPseeker (Yu et al., 2015) was used to annotate the regions in each peak, and global TSS distribution was annotated by using TxDb.Mmusculus.UCSC.mm10.knownGene as reference genome in R (v3.6.1). FeatureCounts (RRID:SCR_012919) were used to quantify the count levels in each peak region. The DESeq2 (RRID:SCR_000154) pipeline was used to detect the significantly differentially expressed peaks with $padj < 0.01$ and $|\log_2\text{-fold change}| > 0.5$. The clusterProfiler (RRID:SCR_016884) was used for GSEA enrichment analysis and set the $pvalueCutoff = 0.05$.

Mass spectrometry (MS) data analysis

All the raw files were searched against the UniProt mouse protein sequence database by using Maxquant (v1.6.15.0). The minimum amino acid length was set to 7. Proteins with a false discovery rate (FDR) < 1% at both protein and peptide levels. The relative quantitative value of the protein is calculated by the following steps:

1. First, after the signal intensity value (I) of the peptide in different samples is transformed by centralization, the relative quantitative value (U) of the peptide in different samples is obtained. The calculation formula is as follows: where i represents the sample and j represents the peptide.

$$U_{ij} = I_{ij} / \text{Mean}(I_j)$$

2. In order to eliminate the systematic error of the sample amount of different samples in the mass spectrometry detection, the relative quantitative value of the peptide needs to be corrected by the median normalization method (NR). Calculated as follows:

$$NR_{ij} = U_{ij} / \text{Median}(U_i)$$

3. The relative quantitative value (R) of the protein is expressed as the median value of the relative quantitative value of the specific peptide corresponding to the protein. The calculation formula is as follows: where k represents the protein, and j represents the specific peptide to which the protein belongs.

$$R_{ik} = \text{Median}(NR_{ij}, j \in k)$$

The differentially expressed proteins with $\log_2\text{FoldChange} > 0.5$ (or < -0.5). To identify functional categories of differentially expressed proteins, Gene ontology and KEGG enrichment analyses were performed using the R package clusterProfiler (RRID:SCR_016884). Pheatmap (RRID:SCR_016418) was used to display heatmaps of the expression levels of differentially expressed proteins.

Single-cell RNA-seq analyses

Libraries were prepared using Chromium Single Cell 3' Reagent Kits v2 according to the manufacturer's protocol (10x Genomics) and were sequenced using an Illumina NovaSeq 6000 sequencing. The exogenous sequences (the constructs for expressing sgRNAs, *Myc*) were added to the reference genome to distinguish the tumor and non-tumor cells. The cellranger (v3.0.0) was used to align clean reads with the mm10 or hg19. The Seurat (Stuart et al., 2019) (v.3.2.0) pipeline was applied to the analysis and visualize the single-cell RNA-seq data. Genes expressed in less than 3 cells were not considered, and cells that mitochondrial ratios were lower than 10% and expressed at least 200 but not more than 6,000 genes were retained for analysis. All data sets were merged by Seurat function 'merge' and 4,000 variable genes identified by 'vst' mode were used to calculate the principal components analysis. t-SNE and DM were used to reduce dimension by considering 30 principal components. The slingshot (Street et al., 2018) was used to construct the development tree and calculate the pseudotime. The dynamically expressed genes were identified by VGAM function with a full model of ' \sim sm.ns(Pseudotime)' and q value higher than $10E-50$ were filtered. Dynamically expressed gene modules were identified by calculating the distance of gene-gene Pearson correlation coefficient in monocle3 (Cao et al., 2019) packages. The expression patterns were visualized by pheatmap (RRID:SCR_016418) package and enrichGO, implemented in clusterProfiler (RRID:SCR_016884), was used to enrich the gene ontology biological process in each module.

Cell cycle analysis

To calculate the cell cycle score in every single cell, cell cycle phase signatures were obtained from the Seurat pipeline (Nestorowa et al., 2016). In each cell of single-cell data, CellCycleScoring was used to calculate G2M scores and S scores.

The gene signature definition

We defined the luminal signature as the average expression of *CYP2J2*, *ERBB2*, *ERBB3*, *FGFR3*, *FOXA1*, *GATA3*, *GPX2*, *KRT18*, *KRT19*, *KRT20*, *KRT7*, *KRT8*, *PPARG*, *UPK1A*, *UPK2* and *XBP1* (Robertson et al., 2017). We defined the squamous signature as the average expression of *CD44*, *CDH3*, *COL17A1*, *DSC3*, *GSDMC*, *KRT1*, *KRT14*, *KRT16*, *KRT17*, *KRT5*, *KRT6A*, *KRT6B*, *KRT6C*, *PI3*, *TGM1* and *TP63*. We defined the terminal squamous signature as *COL17A1*, *DSC1*, *DSC2*, *DSC3*, *IVL*, *KRT14*, *KRT16*, *KRT17*, *KRT5*, *KRT6A*, *KRT6B*, *SPRR1A*, *SPRR1B*, *TGM1*, *TGM3* and *TP63*. The TCGA resistance up signature was the top500 up-regulated genes in progressive groups compared to response groups (p -value < 0.05) (Robertson et al., 2017) (Table S2). SCC-like (squamous cell carcinoma like) signature was the top100 up-regulated genes in the SCC-like subtype compared to other subtypes in urothelial cell carcinoma (Sjödahl et al., 2012) (Table S2). We defined the cell death signature as the average expression of genes in positive regulation of cell death (GO:0010942).

QUANTIFICATION AND STATISTICAL ANALYSIS

All *in vitro* and *in vivo* experiments were analyzed by GraphPad Prism (RRID:SCR_002798) version 9 and two-tailed Student's t test was adopted for quantitative analyses. The numbers of independent experiments, samples or events are indicated in the figure legends. Data are represented as mean \pm standard deviation (SD) or otherwise illustrated in figure legends. For *in vitro* treatment, all samples were randomly divided into vehicle or treatment groups. Blinding was performed for tumor measurements and analysis of organoid numbers and sizes. For *in vivo* treatment, the treatment and vehicle groups were randomized according to their tumor burden before treatment. No data were excluded from the study. Statistical analyses of bioinformatics were performed as described in the Figure legends. Survival was measured using the Kaplan-Meier method.

Supplemental information

Acquired semi-squamization during chemotherapy suggests differentiation as a therapeutic strategy for bladder cancer

Manli Wang, Xuelan Chen, Ping Tan, Yiyun Wang, Xiangyu Pan, Tianhai Lin, Yong Jiang, Bo Wang, Huan Xu, Yuying Wang, Yucen Yang, Jian Wang, Lei Zhao, Jiapeng Zhang, Ailing Zhong, Yiman Peng, Jiajia Du, Qi Zhang, Jianan Zheng, Jingyao Chen, Siqu Dai, Feifei Na, Zhenghao Lu, Jiaming Liu, Xiaonan Zheng, Lu Yang, Peng Zhang, Ping Han, Qiyong Gong, Qian Zhong, Kai Xiao, Hanshuo Yang, Hongxin Deng, Yinglan Zhao, Hubing Shi, Jianghong Man, Maling Gou, Chengjian Zhao, Lunzhi Dai, Zhihong Xue, Lu Chen, Yuan Wang, Musheng Zeng, Canhua Huang, Qiang Wei, Yuquan Wei, Yu Liu, and Chong Chen

FigS1

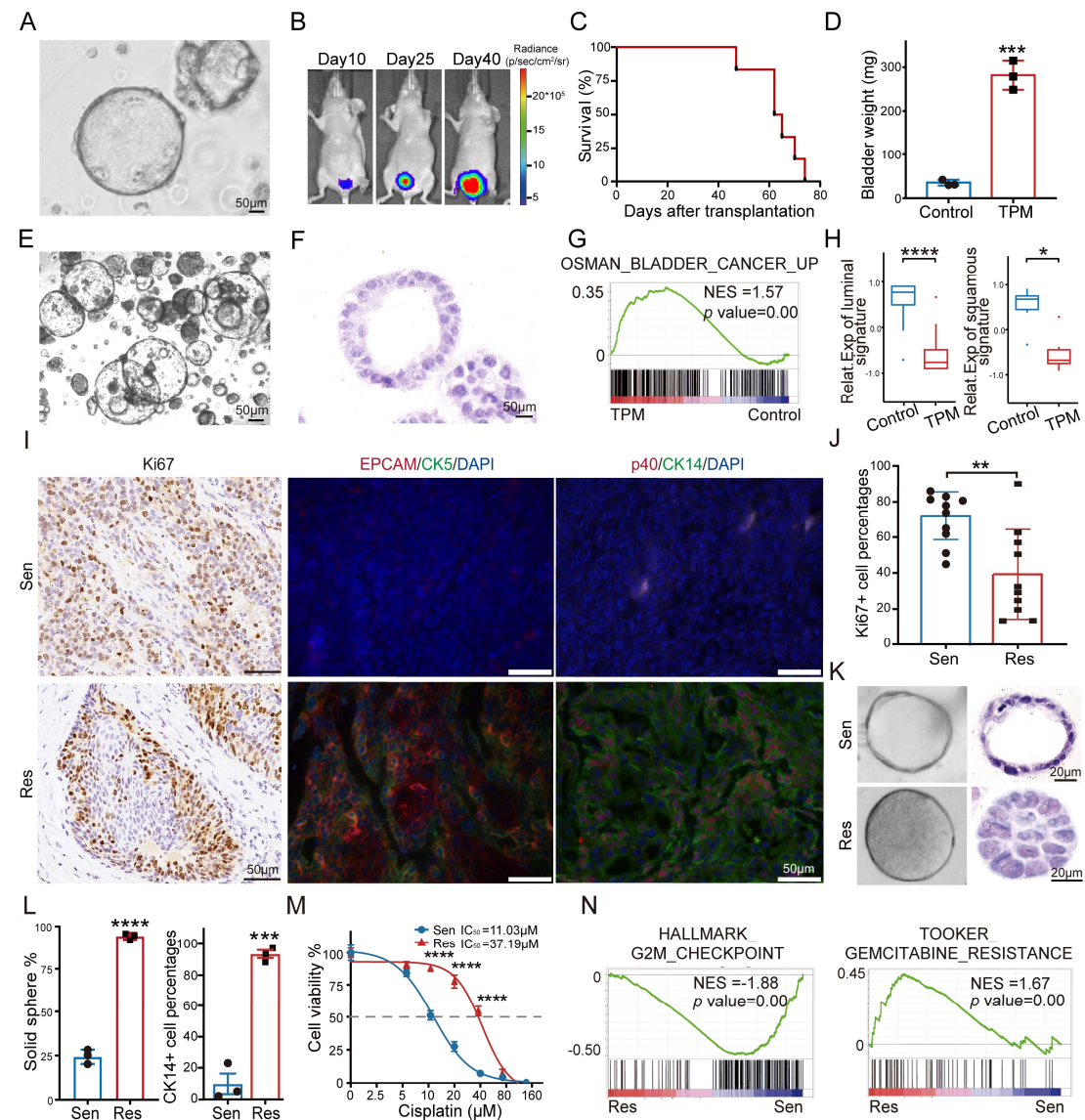


Figure S1. Recapitulating the course of chemotherapy in a new MIBC mouse model, related to Figure 1.

- (A) Bright-field image of mouse normal bladder organoids (representative of n=3 technical replicates). Scale bar, 50µm.
- (B) Bioluminescence images of mice transplanted with Cas9; sgTrp53; sgPten; *Myc* (TPM) organoids (representative of n=6 mice).
- (C) The survival curve of mice transplanted with TPM organoids (representative of n=6 mice).
- (D) The bladder weights of mice transplanted with or without TPM organoids (n=3 mice). ***, $p < 0.001$. Two-sided Student's t test. Data presented as Mean \pm SD.
- (E) Bright-field image of TPM tumor organoids (representative of n=6 mice). Scale bar, 50µm.
- (F) H&E staining of TPM tumor organoids (representative of n=6 mice). Scale bar, 50µm.
- (G) GSEA showing the positive enrichment of the

OSMAN_BLADDER_CANCER_UP in the TPM tumors, compared to normal bladder samples (Control).

- (H) Box plots showing relative expression of luminal signature (left) and squamous signature (right) in normal and TPM tumor organoids (n=3 mice). *, $p < 0.05$; ****, $p < 0.0001$. Two-sided Student's t test. Box plots show the interquartile range (IQR) divided by the median, Whiskers represent the minimum and maximum values at $1.5 \times \text{IQRs}$.
- (I) Images showing IHC staining of Ki67 and IF staining of EPCAM, CK5, p40 and CK14 in sensitive (top) and resistant (bottom) bladder tumors (representative of n=3 mice). Scale bars, $50\mu\text{m}$.
- (J) The percentages of Ki67 positive cells in sensitive and resistant bladder tumors (independent sections of n=3 mice). **, $p < 0.01$. Two-sided Student's t test. Data presented as Mean \pm SD.
- (K) Bright-field and H&E staining of organoids generated from sensitive and resistant tumors (representative of n=3 mice). Scale bar, $20\mu\text{m}$.
- (L) The percentages of solid organoid (left) and CK14 positive cells (right) in sensitive and resistant tumor organoids (independent sections of n=3 mice). ***, $p < 0.001$; ****, $p < 0.0001$. Two-sided Student's t test. Data presented as Mean \pm SD.
- (M) Dose-response curves of cancer organoids from sensitive and resistant tumors treated with cisplatin (n=3 technical replicates). ****, $p < 0.0001$. Two-sided Student's t test.
- (N) GSEA showing negative enrichment of the HALLMARK_G2M_CHECKPOINT (left) and positive enrichment of the TOOKER_GEMCITABINE_RESISTANCE (right) in the resistant tumors, compared to sensitive samples.

FigS2

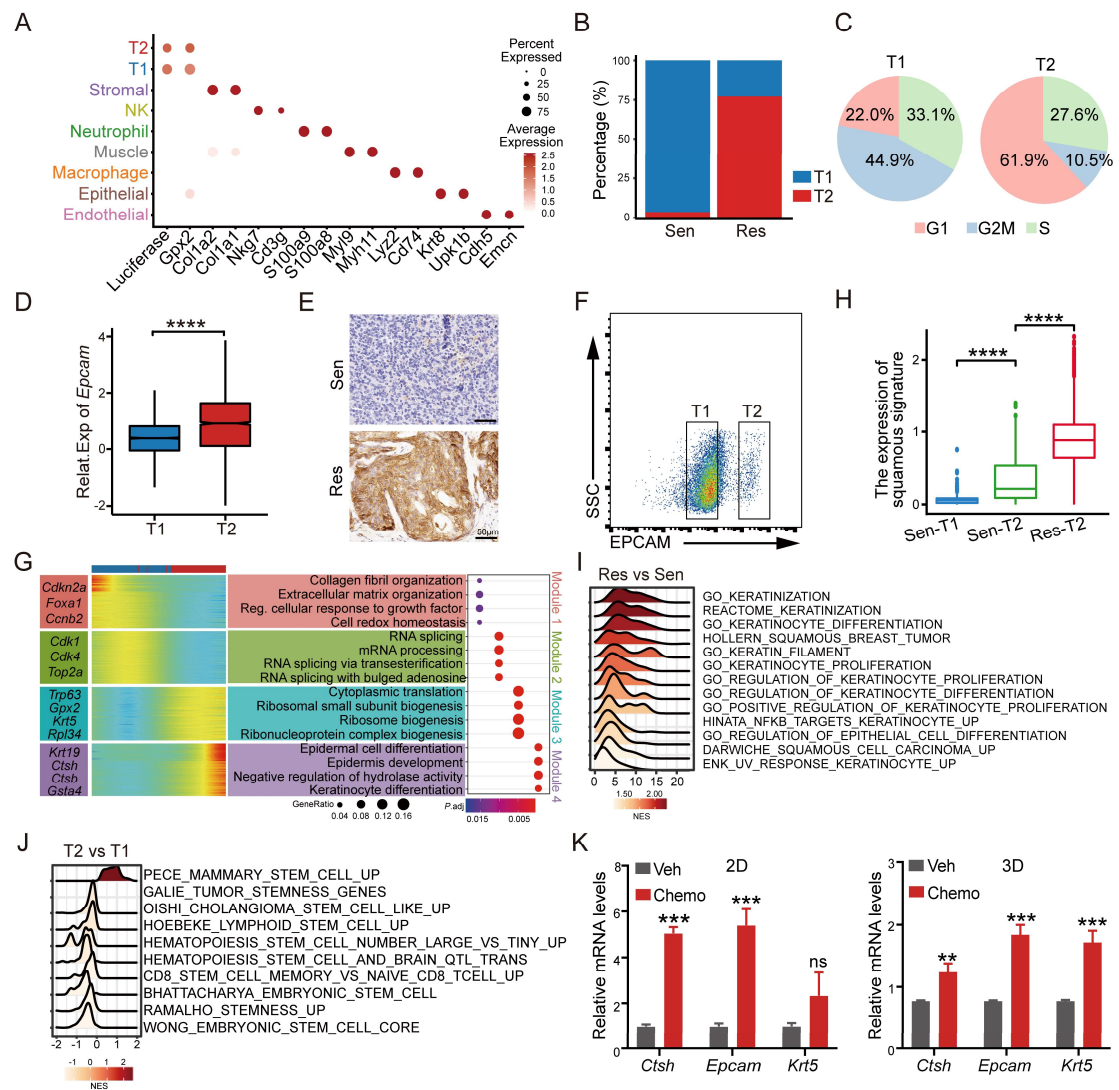


Figure S2. Squamous differentiation as a lineage plasticity for MIBC cells during chemotherapy, related to Figure 2.

- (A) The dot plot showing the marker genes of each cell type in sensitive and resistant mice (n=1 mouse).
- (B) The proportions of T1 and T2 tumor cells in sensitive (sen) and resistant (res) mice.
- (C) The pie charts showing the percentage of cells in different cell cycles in T1 tumors (left) and T2 tumors (right).
- (D) Box plots showing *Epcam* expression in T1 and T2 tumor cells. ****, $p < 0.0001$. Wilcoxon signed-rank test. Box plots show the interquartile range (IQR) divided by the median, Whiskers represent the minimum and maximum values at $1.5 \times \text{IQRs}$.
- (E) EPCAM staining in mouse sensitive and resistant bladder tumors (representative of n=3 mice). Scale bars, 50 μm .
- (F) Flow cytometry plots of T1 and T2 tumor cells in mouse bladder tumors (representative of n=3 mice).
- (G) The dynamically expressed genes on the tumor trajectory, and the GO enrichment plot of the dynamically expressed genes, related to Figure 2E.

- (H) The box plot showing the expression levels of squamous signature in different cell subtypes, measured by scRNA-seq analysis. ****, $p < 0.0001$. Wilcoxon signed-rank test. Box plots show the interquartile range (IQR) divided by the median, Whiskers represent the minimum and maximum values at $1.5 \times \text{IQRs}$.
- (I) The Ridge plot showing the enrichments of squamous and keratinocyte differentiation related pathways in resistant tumors, compared to the sensitive ones analyzed by GSEA, measured by bulk RNA-seq analysis (n=3 mice).
- (J) The Ridge plot showing the stemness-related pathways enrichment in T2, compared to the T1 tumor cells analyzed by GSEA, measured by sc-RNAseq analysis.
- (K) The relative mRNA expressions of *Ctsh*, *Epcam*, and *Krt5* in clones treated with 500 nM cisplatin in 2D and 3D condition (n=3 technical replicates). ns, not significant; **, $p < 0.01$; ***, $p < 0.001$. Two-sided Student's t test. Data presented as Mean \pm SD.

FigS3

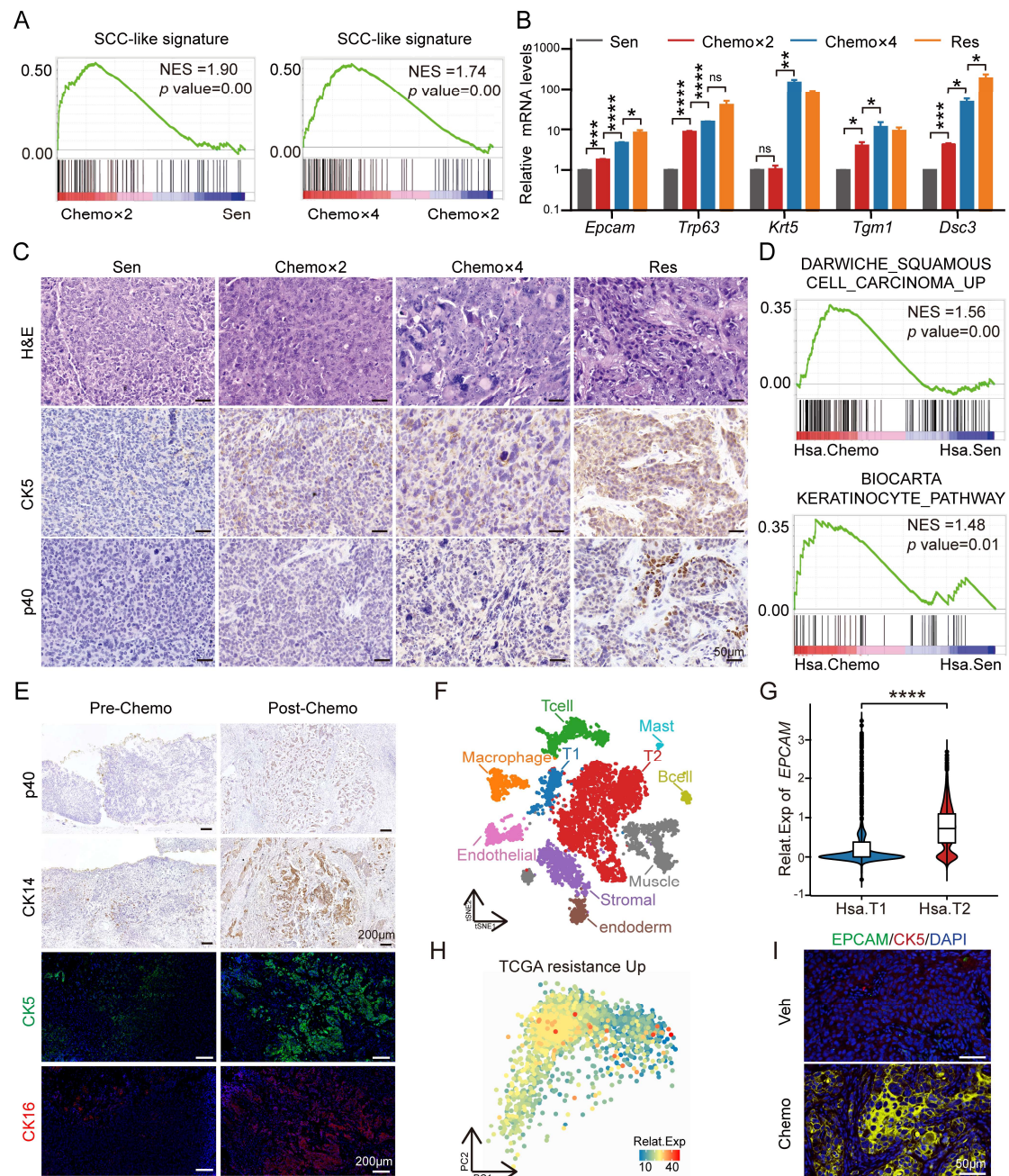


Figure S3. Chemotherapy induces stepwise squamatization in mouse and human MIBC, related to Figure 3.

- (A) GSEA showing positive enrichment of the squamous cell carcinoma like (SCC-like) signature in chemo×2 tumors, compared to sensitive ones (left) and in chemo×4, compared to chemo×2 (right).
- (B) The relative mRNA expressions of *Epcam*, *Trp63*, *Krt5*, *Tgm1*, and *Dsc3* in the sensitive, chemo×2, chemo×4 and resistant mouse bladder tumors (n=3 technical replicates). ns, not significant; *, $p < 0.05$; **, $p < 0.01$; ***, $p < 0.001$; ****, $p < 0.0001$. Two-sided Student's t test. Data presented as Mean \pm SD.
- (C) H&E, CK5, and p40 staining in the sensitive, chemo×2, chemo×4 and resistant mouse bladder tumors (representative of n=3 mice). Scale bars, 50 μ m.

- (D) GSEA showing positive enrichment of the DARWICHE_SQUAMOUS_CELL_CARCINOMA_UP pathway (top), and the BIOCARTA_KERATINOCYTE_PATHWAY (bottom) in the human MIBC PDX models after chemotherapy, compared to sensitive samples.
- (E) Images of p40, CK14, CK5, and CK16 staining in paired pre- or post-chemotherapy tumors from clinical MIBC patients (representative of n=3 patients). Scale bars, 200 μ m.
- (F) The t-SNE map of single-cell RNA-seq analyses of chemosensitive and chemoresistant tumors from human patients, colored by cell subtypes (n=1 patient).
- (G) The violin graph showing the relative expression level of *EPCAM* in human T1 and T2 tumors. ****, $p < 0.0001$. Wilcoxon signed-rank test. Box plots show the interquartile range (IQR) divided by the median, Whiskers represent the minimum and maximum values at 1.5*IQRs.
- (H) The PCA map of human tumor cells, colored by the expression of the TCGA resistance up-regulated genes.
- (I) Images showing EPCAM (green) and CK5 (red) IF staining of sorted human Sen-T1 tumors treated with vehicle or chemotherapy (representative of n=3 mice). Scale bars, 50 μ m.

FigS4

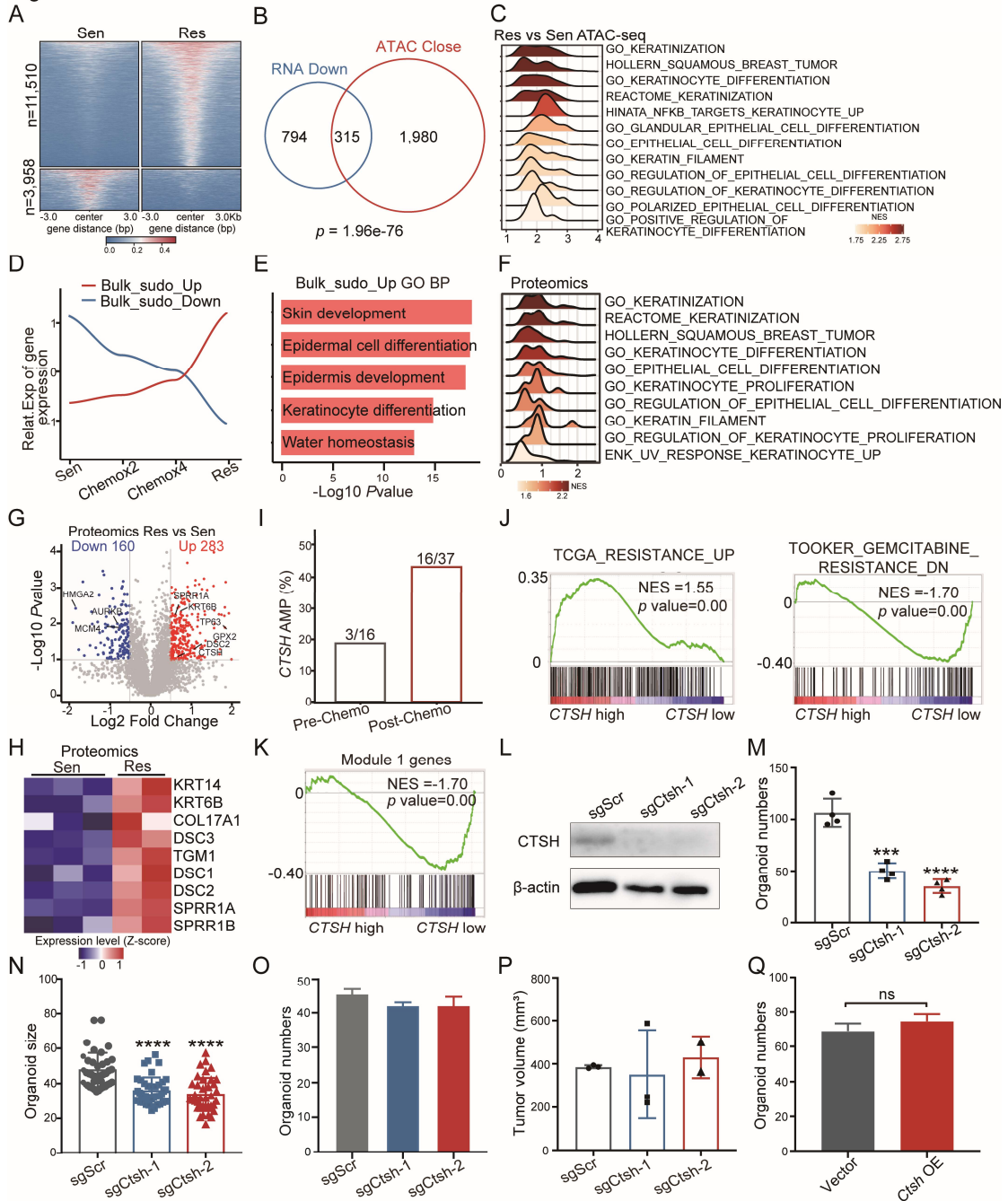


Figure S4. CTSH upregulation is underlying MIBC chemoresistance, related to Figure 4.

- (A) Heatmap showing the chromatin open and close peaks in the mouse chemoresistant tumors, compared to the sensitive ones, measured by ATAC-seq.
- (B) The Venn diagram showing overlapping of the chromatin close genes and those down-regulated in mouse chemoresistant tumors, compared to the chemosensitive ones. Hypergeometric test.
- (C) The Ridge plot showing the GSEA enrichment of squamous and keratin differentiation related pathways in the mouse chemoresistant tumors, compared to the chemosensitive ones, measured by ATAC-seq.
- (D) The gradually up-regulated and down-regulated genes from sensitive to chemo $\times 2$,

chemo×4 and resistant tumors, measured by bulk RNA-seq.

- (E) The GO BP enrichment analysis for the up-regulated genes from sensitive to chemo×2, chemo×4 and resistant tumors, measured by bulk RNA-seq.
- (F) The Ridge plot showing the enrichment of squamous and keratinocyte differentiation pathways in the mouse chemoresistant samples, compared to the chemosensitive samples analyzed by GSEA, measured by MS proteomics assay.
- (G) The volcano plot showing the differentially expressed proteins in chemoresistant tumors, compared to the chemosensitive ones.
- (H) Heatmap showing the relative protein abundance of squamous differentiation-related genes in chemosensitive and chemoresistant samples, measured by MS proteomics assay.
- (I) Bar graph showing the percentages of pre- and post- chemotherapy MIBC samples with *CTSH* amplifications.
- (J) GSEA showing positive enrichment of the TCGA resistance up regulated genes in *CTSH* high BLCA samples, compared to *CTSH* low samples in the TCGA cohort (left). GSEA showing negative enrichment of the *TOOKER_GEMCITABINE_RESISTANCE_DN* genes in the *CTSH* high BLCA samples, compared to *CTSH* low samples in the TCGA cohort (right).
- (K) GSEA showing negative enrichment of the Module1 genes in the TCGA MIBC with *CTSH* high expressions, comparing to those with *CTSH* low expressions.
- (L) Western blotting plots of *CTSH* in mouse chemoresistant tumor organoids with or without *Ctsh* knockout (n=3 independent repeats).
- (M) Organoid numbers of mouse chemoresistant tumor organoids with sgScr or sgCtsh (n=3 independent repeats). ****, $p < 0.0001$; ***, $p < 0.001$. Two-sided Student's t test. Data presented as Mean \pm SD.
- (N) Organoid sizes of mouse chemoresistant tumor organoids with sgScr or sgCtsh (n=3 independent repeats). ****, $p < 0.0001$; ***, $p < 0.001$. Two-sided Student's t test. Data presented as Mean \pm SD.
- (O) The bar graph showing the organoid numbers of mouse chemosensitive tumor organoids with sgScr or sgCtsh (n=3 independent repeats). ns, not significant. Two-sided Student's t test. Data presented as Mean \pm SD.
- (P) The bar graph showing the tumor volumes of mouse chemosensitive tumors with or without *Ctsh* knockout after 3 rounds of chemotherapy (n=3 mice). Two-sided Student's t test. Data presented as Mean \pm SD.
- (Q) The bar graph showing the organoid numbers of mouse chemosensitive tumor organoids with or without *Ctsh* overexpression (n=3 independent repeats). ns, not significant. Two-sided Student's t test. Data presented as Mean \pm SD.

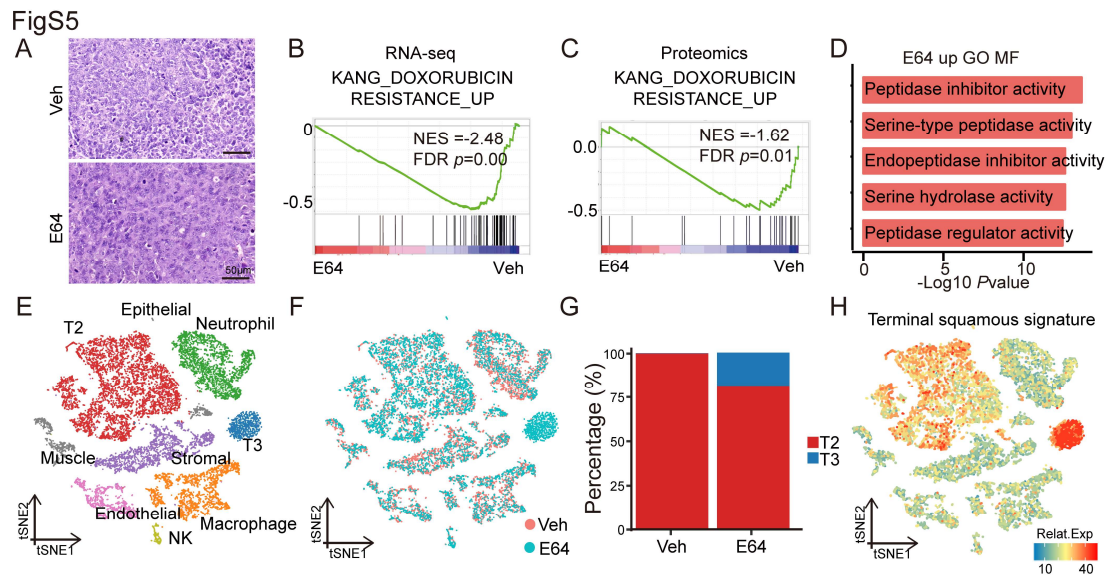


Figure S5. Inhibiting CTSH induces terminal squamous differentiation of chemoresistant MIBC, related to Figure 5.

- (A) Images showing H&E staining of mouse chemosensitive tumors treated with vehicle or E64 (representative of n=4 mice). Scale bars, 50 μ m.
- (B-C) GSEA showing negative enrichment of the KANG_DOXORUBICIN_RESISTANCE_UP pathway in chemoresistant tumor cells treated with E64 compared to those treated with vehicle, measured by RNA-seq analysis (B) or MS (C) proteomics assay.
- (D) GO enrichment analysis for the upregulated genes in Molecular Function term in chemoresistant tumor cells treated with E64 compared to those treated with vehicle, measured by RNA-seq analysis.
- (E) The t-SNE map of single-cell RNA-seq analyses of mouse chemoresistant tumors treated with vehicle or E64, colored by cell subtypes (n=1 mouse).
- (F) The t-SNE map of single-cell RNA-seq analyses of mouse chemoresistant tumors treated with vehicle or E64, colored by sample origins (n=1 mouse).
- (G) The proportions of T2 and T3 tumor cells in chemoresistant tumors treated with vehicle or E64, measured by scRNA-seq analysis.
- (H) The t-SNE map showing the expression of terminal squamous signature genes in mouse chemoresistant tumors treated with vehicle or E64.

Fig S6

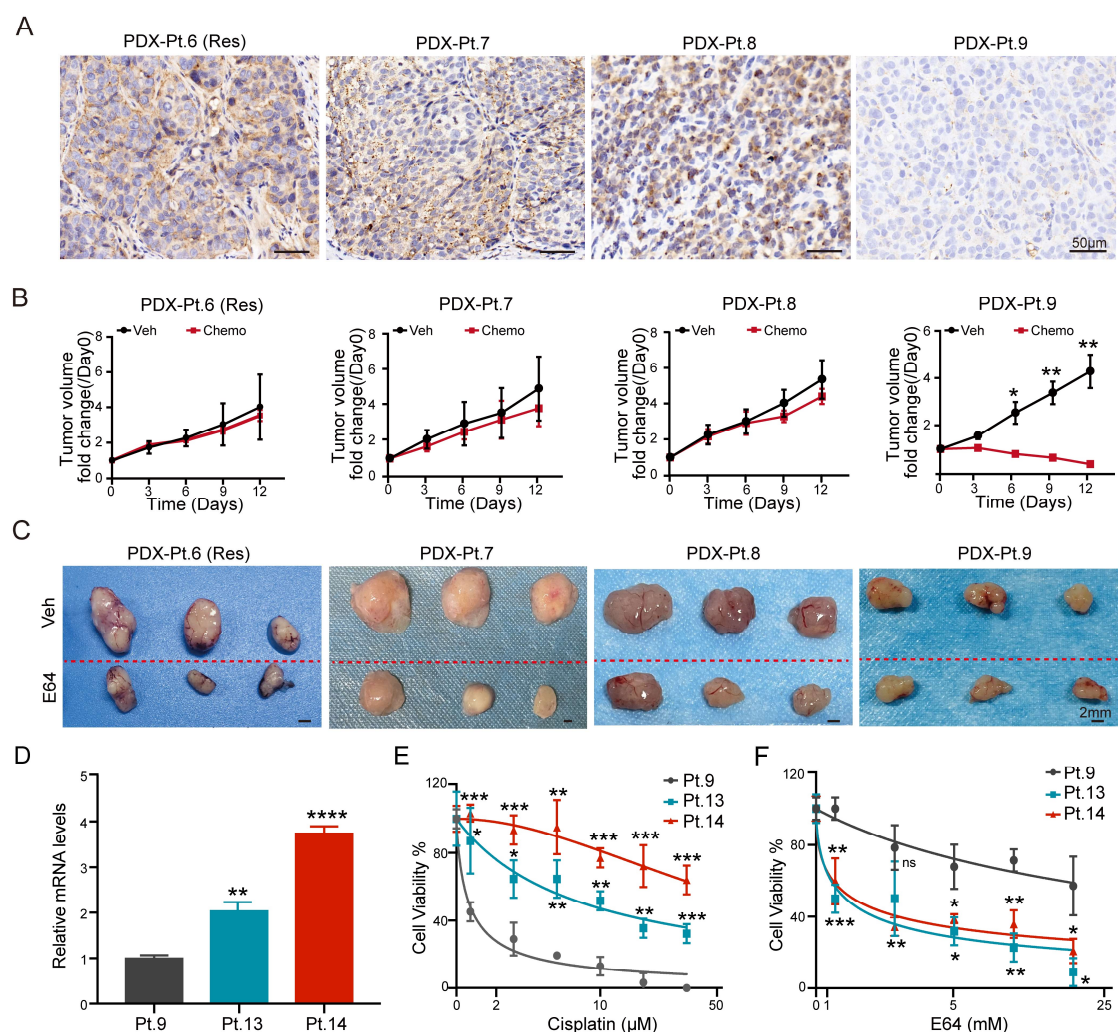


Figure S6. CTSH inhibition specifically represses human chemoresistant MIBC, related to Figure 6.

- (A) CTSH staining in chemoresistant human PDX tumors (Pt.6(Res), 7 and 8) and chemosensitive human PDX tumor (Pt.9) (representative of $n=3$ mice). Scale bars, $50\mu\text{m}$.
- (B) The tumor volume fold change of MIBC PDX from patients 6-9 with vehicle or chemotherapy (Pt.6,7,8: $n=4$ mice; Pt.9: $n=3$ mice). *, $p < 0.05$, **, $p < 0.01$. Two-sided Student's t test. Data presented as Mean \pm SD.
- (C) Images of chemoresistant human PDX tumors (Pt.6 (Res), 7 and 8) and chemosensitive human MIBC PDX (Pt.9) treated with vehicle or E64 (representative of $n=3$ mice). Scale bars, 2mm .
- (D) The relative mRNA levels of *CTSH* in human PDX organoids Pt.9 (sensitive), Pt.13, 14 (resistant) ($n=3$ technical replicates). ** $p < 0.001$; ****, $p < 0.0001$. Two-sided Student's t test. Data presented as Mean \pm SD.
- (E) Dose-response curves of human PDX Pt.9 (sensitive), Pt.13, 14 (resistant) organoids treated with Cisplatin ($n=3$ technical replicates). *, $p < 0.05$; **, $p < 0.01$; ***, $p < 0.001$. Two-sided Student's t test. Data presented as Mean \pm SD.
- (F) Dose-response curves of human PDX Pt.9 (sensitive), Pt.13, 14 (resistant)

organoids treated with E64 (n=3 technical replicates). ns, not significant; *, $p < 0.05$; **, $p < 0.01$; ***, $p < 0.001$. Two-sided Student's t test. Data presented as Mean \pm SD.

Fig S7

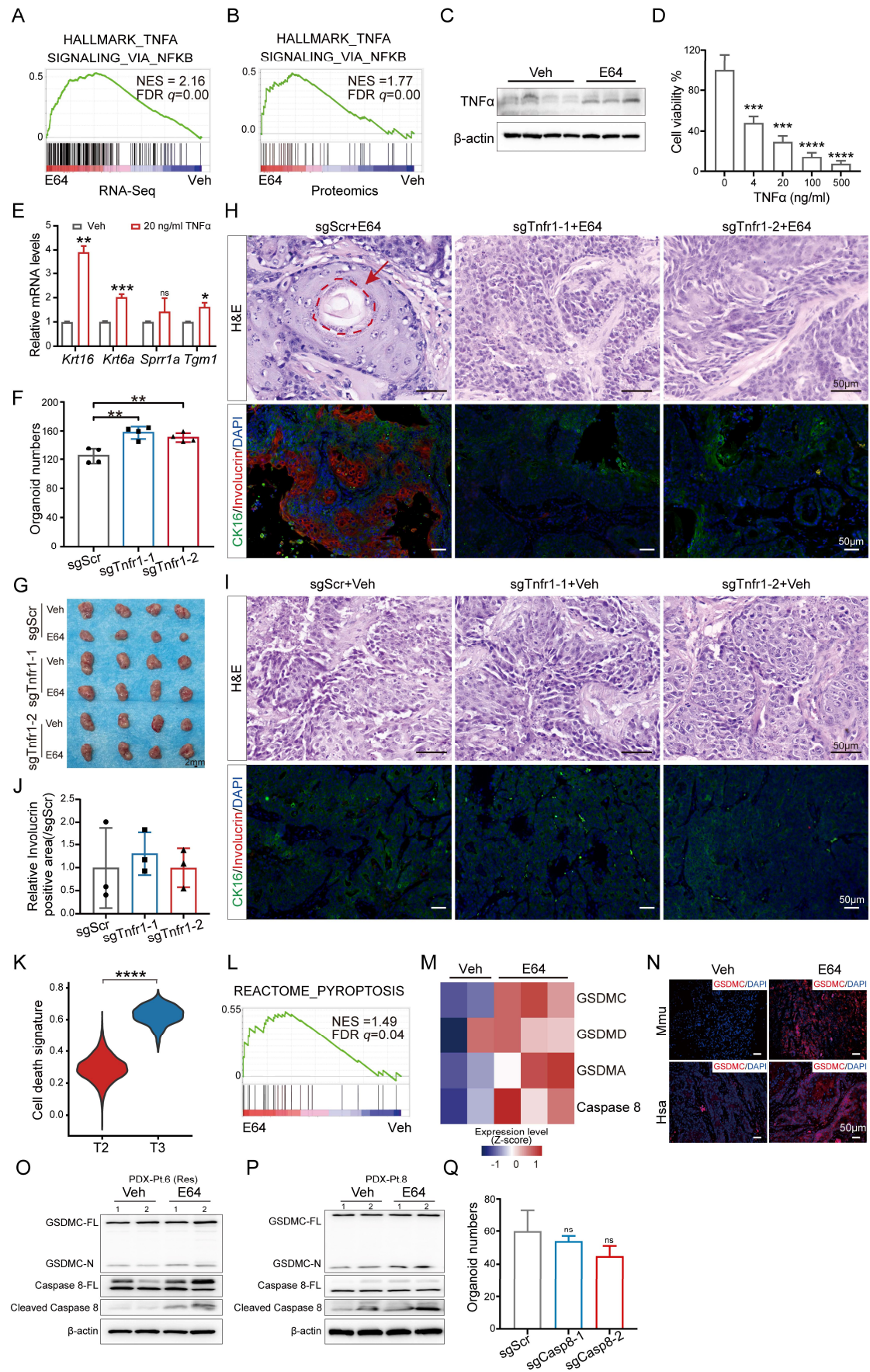


Figure S7. The TNF pathway mediates the differentiation therapy of chemoresistant MIBC, related to Figure 7.

- (A) GSEA showing positive enrichment of the HALLMARK_TNFA_SIGNALING_VIA_NFKB pathway in E64 treated chemoresistant tumors compared to those treated with vehicle, measured by RNA-seq.
- (B) GSEA showing positive enrichment of the HALLMARK_TNFA_SIGNALING_VIA_NFKB pathway in the E64 treated chemoresistant tumors compared to those treated with vehicle, measured by MS proteomics assay.
- (C) Western blotting plots of TNF α in mouse chemoresistant tumors treated with E64 or vehicle (n=3 independent repeats).
- (D) Cell viability of mouse chemoresistant tumor organoids treated with vehicle or TNF α (normalized to vehicle) (n=3 technical replicates). ***, $p < 0.001$; ****, $p < 0.0001$. Two-sided Student's t test. Data presented as Mean \pm SD.
- (E) The relative mRNA levels of *Krt16*, *Krt6a*, *Sprr1a*, *Tgm1* in mouse chemoresistant tumor organoids treated with vehicle or 20 ng/ml TNF α (n=3 technical replicates). ns, not significant; *, $p < 0.05$; **, $p < 0.01$; ***, $p < 0.001$. Two-sided Student's t test. Data presented as Mean \pm SD.
- (F) The organoid numbers of mouse chemoresistant tumors with sgScr or sgTnfr1 (n=4 technical repeats). **, $p < 0.01$. Two-sided Student's t test. Data presented as Mean \pm SD.
- (G) Bright-field image of mouse chemoresistant tumors with sgScr or sgTnfr1 treated with vehicle or E64 (representative of n=4 mice). Scale bar, 2 mm.
- (H) Images showing H&E staining and immunofluorescence staining of CK16 (green) and involucrin (red) of mouse chemoresistant tumors with sgScr or sgTnfr1 treated with E64 (representative of n=4 mice). Scale bars, 50 μ m.
- (I) Images showing H&E staining and immunofluorescence staining of CK16 (green) and involucrin (red) of mouse chemoresistant tumors with sgScr or sgTnfr1 treated with vehicle (representative of n=4 mice). Scale bars, 50 μ m.
- (J) The statistical graph showing the relative involucrin positive staining areas of Figure S7I (independent sections of n=3 mice). Data presented as Mean \pm SD.
- (K) The violin plot shows cell death signature in T2 and T3 tumor cells. ****, $p < 0.0001$. Wilcoxon signed-rank test, measured by scRNA-seq analysis.
- (L) GSEA showing positive enrichment of the REACTOME_PYROPTOSIS pathway in the E64-treated chemoresistant tumors compared to those treated by vehicle, measured by RNA-seq.
- (M) Heatmap showing the relative protein levels of pyroptosis-related genes in the chemoresistant tumors with vehicle (n=2 mice) or E64 treatment (n=3 mice).
- (N) Immunofluorescence staining of GSDMC (red) in mouse and human chemoresistant tumors treated with vehicle or E64 (n=3 mice). Scale bars, 50 μ m.
- (O) Western blotting plots of GSDMC and Caspase 8 in chemoresistant PDX treated with vehicle or E64 (Patient 6) (n=3 independent repeats).
- (P) Western blotting plots of GSDMC and Caspase 8 in chemoresistant PDX treated

with vehicle or E64 (Patient 8) (n=3 independent repeats).

- (Q) Organoid numbers of mouse chemoresistant tumor organoids edited with sgScr or sgCasp8 (n=3 technical repeats). ns, not significant. Two-sided Student's t test. Data presented as Mean \pm SD.